Astronomy & Astrophysics manuscript no. electrons
February 9, 2010

Galactic electrons and positrons at the Earth: new estimate of the primary and secondary fluxes

T. Delahaye[1,2], J. Lavalle[2], R. Lineros[2], F. Donato[2], and N. Fornengo[2]

[1] LAPTH, Université de Savoie & CNRS, BP 110, F-74941 Annecy-le-Vieux Cedex — France.
[2] Dipartimento di Fisica Teorica, Università di Torino & INFN - Sezione di Torino, Via Giuria 1, I-10122 Torino — Italia.

Received / Accepted

ABSTRACT

Context. The so-called excess of cosmic ray (CR) positrons observed by the PAMELA satellite up to 100 GeV has opened windows for various interpretations involving standard astrophysics and/or a possible exotic contribution from dark matter annihilation or decay. The subsequent Fermi data on CR electrons plus positrons in the range 0.02-1 TeV, and HESS data above 1 TeV have provided additional information on the leptonic content of local Galactic CRs.
Aims. In this paper, we wish to revisit the full predictions of the so-called *standard* CR lepton fluxes at the Earth of both secondary and primary origins, evaluate the theoretical uncertainties, and determine their level of consistency with respect to the available data.
Methods. For propagation, we use a relativistic treatment of the energy losses for which we provide useful parameterizations. We compute the secondary components by improving on the method that we derived earlier for positrons (Delahaye et al., 2009). For primaries, we estimate the contributions from standard astrophysical sources (supernova remnants and pulsars) by considering all known local objects within 2 kpc and a smooth distribution beyond, and investigate the impact of the uncertainties affecting their modeling. For both secondaries and primaries, we further size up the theoretical error due to pure propagation effects.
Results. We find that the electron flux in the energy range 5-30 GeV is well reproduced from a smooth distant distribution of sources with index $\gamma \sim 2.3 - 2.4$, while local sources dominate at higher energy. For positrons, local pulsars have important effect above 5-10 GeV. Uncertainties affecting the source modeling and propagation are degenerate and each translates into about one order of magnitude error in terms of local flux. The spectral shape at high energy is barely connected with the spectral indices of local sources, more with the hierarchy in their distance, age and power. Still, our global and self-consistent analysis can fairly explain all available data, without over-tuning the parameters.
Conclusions. Our results show that though a *standard paradigm* of Galactic CRs is well established, we can hardly talk about any *standard model* of CR leptons, because of the very large theoretical uncertainties. Our analysis provides details on the impact of these uncertainties, thereby sketching a roadmap for further improvements.

Key words. (ISM:) cosmic rays

Preprint DFTT 51/2009 and LAPTH-1339/09

1. Introduction

Cosmic ray (CR) electrons and positrons[1] make $\sim 1\%$ of the CR budget at the Earth in the GeV-TeV energy scale, and are very interesting messengers to probe the acceleration processes in CR sources, propagation phenomenology and the interstellar environment itself, complementary to protons (*e.g.* Blandford & Eichler 1987). At energies $\gtrsim 100$ GeV, they are featured by the very local environment. Indeed, their typical propagation scale is limited to the kpc scale due to very efficient electromagnetic energy losses resulting from Compton scattering with the interstellar radiation fields (ISRF), the cosmic microwave background (CMB) and the magnetic field (Jones 1965; Blumenthal & Gould 1970). High energy CR electrons can be produced directly at sources, the well-known standard CR accelerators being supernova remnants (SNRs) and pulsars, in which case they are referred to as *primary* electrons. They can also be created out of secondary processes, mostly nuclear interactions of cosmic protons and light nuclei with the interstellar medium (ISM) gas concentrated in the Galactic disk (spallation), in which case they are referred to as *secondary* electrons. Because they were thought barely produced in standard astrophysical sources, positrons have been proposed as potential tracers of new physics, in particular the annihilation or decay of dark matter (Silk & Srednicki 1984). Although the main theoretical ideas regarding the origin and propagation of cosmic electrons have been formalized for a long time in the seminal monograph of Ginzburg & Syrovatskii (1964), their current measurements are still far from being completely understood.

The recent observation by the PAMELA satellite (Adriani et al. 2009) of a rising positron fraction up

Send offprint requests to:
delahaye@lapp.in2p3.fr
lavalle@to.infn.it
lineros@to.infn.it

[1] Hereafter, *electrons* will denote both electrons and positrons, unless specified.

to ∼100 GeV has triggered a considerable amount of interpretation attempts. Estimates of the cosmic electron and positron fluxes were first calculated in details in Moskalenko & Strong (1998), where only secondaries were considered for positrons, which fails to match the data. We have recently derived novel predictions of the secondary positron flux at the Earth, with a particular focus on sizing the theoretical errors coming from uncertainties in spallation cross sections, in the modeling of the progenitor interstellar (IS) CR flux, in the characterization of the energy losses and on the propagation parameters (Delahaye et al. 2009). Although the overall theoretical uncertainty is of about one order of magnitude, we have still shown that a rising positron fraction was not expected unless a very soft electron spectrum was considered. Even in that case, however, we have also illustrated how difficult it was to accommodate a good fit to the PAMELA data in spectral shape as well as in amplitude. Anyway, such a soft electron spectrum is at the lowest statistical edge of the current electron cosmic ray data below 30 GeV. Likewise, it is not supported by the unprecedented measurements recently performed with the Fermi satellite between 20 GeV and 1 TeV of CR electrons plus positrons (Abdo et al. 2009b), which sets the true denominator of the positron fraction. At this stage, separate data of positrons and electrons would be of particular interest and would provide stronger grounds to any interpretation attempt, but are not yet available, unfortunately. Anyway, from both predictions of the secondary positron flux and the current data, it appears unlikely that this increase observed in the positron fraction is of pure secondary origin. Therefore, this positron excess points towards the existence of primary sources of positrons in the neighborhood. Note finally that the cutoff in the electron flux recently observed by HESS around 3 TeV provides a very interesting and complementary information (Aharonian et al. 2008).

It has long been demonstrated that standard astrophysical sources could afford for this extra-yield of cosmic positrons. For instance, as early discussed by Boulares (1989) (see also *e.g.* Aharonian et al. 1995; Chi et al. 1996; Zhang & Cheng 2001), pulsars could provide sizable contributions to the positron flux from pair conversions of γ-rays in the strong magnetic fields that they host. Such an idea was recently revisited by several authors (*e.g.* Hooper et al. 2009; Yüksel et al. 2009; Profumo 2008; Malyshev et al. 2009), who drew similar conclusions. Another class of standard contributions invokes spallation processes with the ISM gas during the acceleration stage of cosmic rays inside SNRs that were not considered before (Blasi 2009; Mertsch & Sarkar 2009; Ahlers et al. 2009). This hypothesis leads to the additional production of antiprotons, which provides an interesting counterpart (Blasi & Serpico 2009), making it testable in the near future. Let us finally mention that using a more refined spatial distribution of sources and of interstellar gas might also lead to a rising positron fraction in the PAMELA energy range (Shaviv et al. 2009).

The large amount of standard, but still different, astrophysical interpretations of the observed positron fraction is noteworthy and points chiefly towards significant lacks in our understanding of the cosmic electron production in sources and their subsequent propagation in the Galaxy. This also means that invoking a *standard model of Galactic cosmic rays* is still hardly conceivable in spite of the progresses achieved so far in the description of cosmic ray sources, propagation and interaction with the ISM and ISRF. Because high energy electrons have a propagation horizon much smaller than light cosmic ray nuclei, they offer, however, interesting means to test the consistency of the overall phenomenological modeling; the Galactic environment is indeed much better constrained locally.

Our purpose is to contribute novel calculations of the electron and positron fluxes in order to assess the relative roles of the different primaries and secondaries in the positron fraction. This is somehow a continuation of the study that we recently performed on secondary positrons (Delahaye et al. 2009). We will treat all of these components in a self-consistent framework that includes *e.g.* improved propagation modeling (with a full relativistic treatment of the energy losses) as well as constrained properties of local sources, including both SNRs and pulsars. Not only does this study aim to improve and clarify the interpretation of the PAMELA data from standard astrophysical processes, but it will also help to check whether the cosmic positron spectrum still offers interesting windows to search for new physics. A particularly important issue is whether positrons injected from dark matter annihilation could be disentangled from all other standard contributions. Indeed, dark matter could in some cases manifests itself in this channel (*e.g.* Baltz & Edsjö 1998; Hooper & Kribs 2004; Lavalle et al. 2007; Asano et al. 2007; Bergström et al. 2008; Cirelli et al. 2008; Delahaye et al. 2008; Pieri et al. 2009; Catena et al. 2009), and the discovery of an exotic contribution to the positron budget would be a spectacular result. Yet, any such result will have to rely on solid grounds, in particular a good understanding of the standard astrophysical contributions. We will show that the theoretical uncertainties are very large, and will discuss in details the relative impact of each ingredient. Such a variance in the predictions is quite bad news for exotic searches, since the background is not under control. Moreover, despite these uncertainties, we will show that our calculations, involving pure standard astrophysical processes in a self-consistent framework, can very well explain the whole set of available data on CR leptons, without over-tuning the parameters, and therefore without any need of exotic physics.

The outline of the paper is the following. In Sect. 2, we will describe in details our propagation model, with a particular focus on the relativistic treatment of the energy losses. In Sect. 3, we will revisit the predictions of the local secondary electron and positron fluxes and discuss the effects of our improved propagation model compared to the results we recently derived in Delahaye et al. (2009). In Sect. 4, we will compute the primary electron component by considering a smooth distribution of SNRs beyond ~ 2 kpc from the Earth, and by determining the contribution of each known SNR within this distance; we will discuss in detail the impact of the source modeling. In Sect. 5, we will shortly revisit the primary positrons that pulsars could generate by using the same approach as for electrons. We will finally compare our results with all available data on CR leptons in Sect. 6, before concluding in Sect. 7.

2. Propagation of electrons and positrons

2.1. General aspects

CR propagation in the Galaxy involves quite complex processes. The spatial diffusion is due to convection upwards and downwards the Galactic disk and to the erratic bouncing of CRs off moving magnetic inhomogeneities, which also induces a diffusion in momentum space, more precisely diffusive reacceleration. Energy losses along the CR journey add another feature in the diffusion in momentum space. Nuclei can also experience nuclear interactions (spallation); this is of course irrelevant for electron propagation, but spallation will still be considered as the source of secondaries. The propagation zone spreads beyond the disk, and is very often modeled as a cylindrical slab of radius $R \simeq R_{\rm disk} \simeq 20$ kpc, and a vertical half-height of $L \simeq 1-15$ kpc. Standard sources of CRs and the ISM gas are mostly located within the disk which has a vertical extent of $z_{\rm disk} \simeq 0.1$ kpc. More details on propagation phenomenology can be found in (*e.g.* Berezinskii et al. 1990; Longair 1994; Strong et al. 2007).

Throughout this paper, we will discuss high energy electrons with particular interest on energies above ~ 10 GeV, for which the effects of solar modulation are much weaker. We have demonstrated in (Delahaye et al. 2009) that convection and reacceleration could be neglected above a few GeV, so that the propagation of electrons can be expressed in terms of the usual current conservation equation $\widehat{\mathcal{D}}\mathcal{N} = \mathcal{Q}(E,\boldsymbol{x},t)$, where the transport operator $\widehat{\mathcal{D}}$ can be expanded as follows:

$$\partial_t \mathcal{N} - \boldsymbol{\nabla}\cdot\{K(E)\boldsymbol{\nabla}\mathcal{N}\} + \partial_E\left\{\frac{dE}{dt}\mathcal{N}\right\} = \mathcal{Q}(E,\boldsymbol{x},t)\ . \quad (1)$$

The electron number density per unit of energy is denoted $\mathcal{N} = \mathcal{N}(E,\boldsymbol{x},t) \equiv dn/dE$, $K(E)$ is the energy-dependent diffusion coefficient assumed isotropic and homogeneous, dE/dt is the energy loss term and $\mathcal{Q}$ is the source term. As mentioned above, we have neglected convection and reacceleration.

The above equation can be solved numerically, *e.g.* by means of the public code `GALPROP` (Strong & Moskalenko 1998), which is aimed at treating CR nuclei and electrons in the same framework. However, it turns out that most of the studies using this code do not usually correlate the features of protons at sources to those of electrons (*e.g.* Moskalenko & Strong 1998; Strong et al. 2000), which rather alleviates the relevance of treating nuclei and electrons in the same global numerical framework. Indeed, one can always, in that case, tune the source modeling differently for each of these species to accommodate the observational constraints.

We have adopted instead a semi-analytical propagation modeling which is aimed at surveying a wider parameter space and which makes easier and clearer the discussion on theoretical uncertainties. Analytical steady state solutions to Eq. (1), in terms of Green functions, can be found in (*e.g.* Bulanov & Dogel 1974; Berezinskii et al. 1990; Baltz & Edsjö 1998; Lavalle et al. 2007; Delahaye et al. 2008) in the non-relativistic Thomson approximation of the inverse Compton energy losses. We will improve this model by including a full relativistic calculation of the energy losses (see Sect. 2.4) and the time-dependent solution to Eq. (1) which will come when dealing with local sources (see Sect. 2.2). Anyway, the propagation parameters will still be constrained as usual, by means of the ratio of secondary to primary stable nuclei, except for the energy loss parameters that will be constrained from the description of the local ISRF and magnetic field. This latter point will be discussed in detail in Sect. 2.5.

For the sake of completeness, let us briefly recall the Green functions that can be worked out as steady state solutions to Eq. (1), disregarding the energy loss features for the moment. Assuming that spatial diffusion and energy losses are isotropic and homogeneous, it is an academic exercise to derive the steady state Green function in an infinite 3D space, which obeys $\widehat{\mathcal{D}}_{\bar{t}}\,\mathcal{G} = \delta^3(\boldsymbol{x}-\boldsymbol{x}_s)\delta(E-E_s)$:

$$\mathcal{G}(\boldsymbol{x},E\leftarrow\boldsymbol{x}_s,E_s) = \frac{1}{b(E)\,(\pi\,\lambda^2)^{\frac{3}{2}}}\cdot\exp\left\{\frac{(\boldsymbol{x}_s-\boldsymbol{x})^2}{\lambda^2}\right\}\ , \quad (2)$$

where s indexes the source ($E_s \geq E$), and where we have defined the energy loss rate and the diffusion scale as follows:

$$b(E) \equiv -\frac{dE}{dt}\ ;\ \ \lambda^2 \equiv 4\int_E^{E_s} dE'\frac{K(E')}{b(E')}\ . \quad (3)$$

The propagation scale λ characterizes the CR electron horizon and depends on energy through the ratio of the diffusion coefficient to the energy loss rate. If these are both described by power laws, *e.g.* $K(E)\propto E^\delta$ and $b(E)\propto E^\alpha$, then $\mathcal{G}\propto E^{\frac{\alpha}{2}-\frac{3}{2}(\delta+1)}$; this will have importance when discussing the primary and secondary contributions later on. For definiteness, we define:

$$\begin{aligned} K(E) &\equiv \beta\,K_0\left(\frac{\mathcal{R}}{1\,\mathrm{GV}}\right)^\delta \simeq K_0\,\epsilon^\delta \\ b(E) &\equiv b_0\,\epsilon^\alpha = \frac{E_0}{\tau_l}\,\epsilon^\alpha \ \text{ with }\ \epsilon\equiv\frac{E}{E_0=1\,\mathrm{GeV}}\ , \end{aligned} \quad (4)$$

where K_0 and b_0 are the normalizations of the diffusion coefficient and of the energy loss rate, respectively, that carry the appropriate dimensions. τ_l is the characteristic energy loss time.

Because of the finite spatial extent of the diffusion slab, boundary conditions must be taken into account when the propagation scale is of order of the vertical or radial boundaries. At the Earth location, that we will fix to $(x_\odot,y_\odot,z_\odot) = (8,0,0)$ kpc throughout the paper, the radial boundary is irrelevant while $(R-r_\odot) \gtrsim L$, which is almost always the case for reasonable values of L and R, as constrained by observations (*e.g.* Strong & Moskalenko 1998; Maurin et al. 2001). Therefore, we can shortly review the solutions accounting for the the vertical boundary condition only. In that case, one can split the general Green function into two terms, one radial and another vertical, such as $\mathcal{G} = (\mathcal{G}_r\times\mathcal{G}_z)/b(E)$. The radial term is merely the infinite 2D solution:

$$\mathcal{G}_r(\boldsymbol{r},E\leftarrow\boldsymbol{r}_s,E_s) = \frac{1}{\pi\,\lambda^2}\exp\left\{-\frac{(\boldsymbol{r}-\boldsymbol{r}_s)^2}{\lambda^2}\right\}\ , \quad (5)$$

where $\boldsymbol{r}$ is the projection of the electron position in the $z=0$ plane, and s indexes the source. The vertical solution can be determined by different methods. For small propagation scale, more precisely for $\lambda < L$, one can use the image method (*e.g.* Cowsik & Lee 1979; Baltz & Edsjö 1998):

$$\mathcal{G}_z(z,E\leftarrow z_s,E_s) = \sum_{n=-\infty}^{+\infty}\frac{(-1)^n}{\sqrt{\pi}\lambda}\exp\left\{-\frac{(z-z_{s,n})^2}{\lambda^2}\right\}\ , \quad (6)$$

where $z_{s,n} \equiv 2\,n\,L + (-1)^n z_s$. For larger propagation scale, *i.e.* $\lambda \gtrsim L$, it turns out that using the basis defined by the Helmholtz eigen-functions allows a better numerical convergence (Lavalle et al. 2007). In that case, we have instead:

$$\mathcal{G}_z(z, E \leftarrow z_s, E_s) \;=\; \frac{1}{L}\sum_{n=1}^{+\infty}\left\{ e^{-\left[\frac{k_n \lambda}{2}\right]^2} \phi_n(z)\phi_n(z_s) + e^{-\left[\frac{k'_n \lambda}{2}\right]^2} \phi'_n(z)\phi'_n(z_s) \right\}, \qquad (7)$$

where the pair and odd eigen-modes and eigen-functions read, respectively:

$$\begin{aligned} k_n &= (n-1/2)\pi/L \;\;;\;\; k'_n = n\pi/L\,; \\ \phi_n(z) &= \sin\left(k_n(L-|z|)\right) \;\;;\;\; \phi'_n(z) = \sin\left(k'_n(L-z)\right)\,. \end{aligned} \qquad (8)$$

The radial boundary condition becomes relevant when $(R - r_\odot) \sim L \sim \lambda$. We have accounted for it by means of the image method for the radial component, or, since the smooth source term exhibits a cylindrical symmetry, by expanding the solution in terms of Bessel series (see *e.g.* Bulanov & Dogel 1974; Berezinskii et al. 1990; Delahaye et al. 2008). The radial boundary condition will be, however, mostly irrelevant in the following, since we will mainly consider electron energies $\gtrsim 10$ GeV, for which the propagation scale is not more than a few kpc.

2.2. Time-dependent solution

The steady-state solutions derived above are safe approximations for a continuous injection of CRs in the ISM, as it is the case for secondaries. In opposition, primary CRs are released after violent and localized events like supernova explosions, the remnants and sometimes pulsars of which are thought to be the most common Galactic CR accelerators. Since the supernova explosion rate $\Gamma_\star$ is likely of a few per century, the CR injection rate could exhibit significant local variations over the CR lifetime (confinement time, or energy loss time, depending on the species) provided this latter is much larger than the individual source lifetime. Since electrons lose energy very efficiently, there is a spatial scale (an energy scale, equivalently), below (above) which these local variations will have a significant effect on the local electron density. To get a rough estimate of this scale, one can compare the energy loss rate $b(E)$ with the *local* injection rate. Assuming that source events are all identical and homogeneously distributed in an infinitely thin disk of radius $R = 20$ kpc, local fluctuations are expected to be smoothed when integrated over an electron horizon λ such that $\Gamma_\star(\lambda/R)^2 \gg b(E)/E$. Using $K_0 \approx 0.01\,\mathrm{kpc}^2/\mathrm{Myr}$, $b(E) \approx (\mathrm{GeV/Myr}/315)\epsilon^2$ and $\Gamma_\star \approx 1/100\,\mathrm{yr}$, we find $E \ll 80$ GeV, which means that local fluctuations of the flux are likely important above a few tens of GeV. A similar reasoning was in fact emphasized a few decades ago by Shen (1970). Anyway, it is worth recalling that a significant number of SNRs and pulsars is actually observed within a few kpc to the Earth. We can therefore hope that current measurements will help to feature them as electron sources, and thereby provide grounds to predict the local electron density.

To estimate the contribution of local transient sources, we need to solve the full time-dependent transport Eq. (1), and we will further show that the method used for the steady-state case can also be used, though partly, for the transient case. The time-dependent Green function, $\mathcal{G}_t$, is again defined by means of the transport operator, asking that $\widehat{\mathcal{D}}\,\mathcal{G}_t = \delta^3(\boldsymbol{x} - \boldsymbol{x}_s)\delta(E - E_s)\delta(t - t_s)$. The general procedure to solve this equation is to work in Fourier space (*e.g.* Ginzburg & Syrovatskii 1964; Berezinskii et al. 1990; Atoyan et al. 1995; Kobayashi et al. 2004; Baltz & Wai 2004), using

$$\mathcal{G}_t(t, E, \boldsymbol{x}) \;=\; \frac{1}{(2\pi)^2}\iint d^3k\, d\omega \times \exp\left\{i\big(\boldsymbol{k}\cdot\boldsymbol{x} + \omega t\big)\right\}\,\phi(\omega, E, k)\,. \qquad (9)$$

In Fourier space, we now get an ordinary differential equation on E for each pair (ω, k),

$$\left\{i\omega + k^2 K(E)\right\}\phi - \partial_E\Big(b(E)\phi\Big) \;=\; \delta(E - E_s) \times \frac{1}{(2\pi)^2}\exp\left\{-i(\boldsymbol{k}\cdot\boldsymbol{x}_s + \omega t_s)\right\}, \qquad (10)$$

that is solved by:

$$\phi(\omega, E, k) = \frac{1}{b(E)}\frac{1}{(2\pi)^2}\exp\left\{-\frac{1}{4}k^2\lambda^2 - i\boldsymbol{k}\cdot\boldsymbol{x}_s\right\} \times \exp\left\{-i\omega(t_s + \Delta\tau)\right\}. \qquad (11)$$

This solution is only valid for $E \leq E_s$ because it describes processes ruled by energy losses. It contains the propagation scale λ previously defined in Eq. (3) and the *loss time* defined as

$$\Delta\tau(E, E_s) \equiv \int_E^{E_s} \frac{dE'}{b(E')}\,. \qquad (12)$$

This loss time corresponds to the average time that a particle needs to see its energy decreased from E_s to E because of losses. The inverse Fourier transformation is straightforward from Eq. (9), and we eventually obtain:

$$\mathcal{G}_t(t, E, \boldsymbol{x} \leftarrow t_s, E_s, \boldsymbol{x}_s) = \frac{\delta(\Delta t - \Delta\tau)}{b(E)}\frac{\exp\left\{-\frac{(\boldsymbol{x}-\boldsymbol{x}_s)^2}{\lambda^2}\right\}}{(\pi\lambda^2)^{3/2}}\,, \qquad (13)$$

where $\Delta t = t - t_s$, and where one recognizes the steady-state solution times a delta function mixing real time and loss time. Like in the steady-state case, we can further account for the vertical boundary condition by expanding this 3D solution by means of the image method or in the basis of Helmholtz eigen-functions. The final result can therefore be expressed in terms of the full steady-state solution

$$\mathcal{G}_t(t, E, \boldsymbol{x} \leftarrow t_s, E_s, \boldsymbol{x}_s) = \delta(\Delta t - \Delta\tau)\,\mathcal{G}(E, \boldsymbol{x} \leftarrow E_s, \boldsymbol{x}_s) \qquad (14)$$

A complementary interpretation of the time dependence emerges when the temporal delta function is converted into an energy delta function, which is shown convenient for bursting sources for which Δt is fixed. In this case, the Green function reads instead:

$$\mathcal{G}_t(t, E, \boldsymbol{x} \leftarrow t_s, E_s, \boldsymbol{x}_s) \;=\; \delta(E_s - E^\star)\,b(E^\star) \times\mathcal{G}(E, \boldsymbol{x} \leftarrow E_s, \boldsymbol{x}_s)\,, \qquad (15)$$

where the energy $E^\star$ satisfies:

$$\Delta\tau(E, E^\star) = \Delta t \,. \tag{16}$$

Thus, $E^\star$ corresponds to the injection energy needed to observe a particle with energy E after a time $\Delta t = t - t_s$. Although there is no analytical solution to this equation in the full relativistic treatment of the energy losses (see Sect. 2.4), it is still worth working it out in the Thomson approximation:

$$\begin{aligned} E^\star &\underset{\text{approx.}}{\overset{\text{Th.}}{=}} \frac{E}{1 - E/E^{\rm Th}_{\rm max}} \\ \text{with } E^{\rm Th}_{\rm max} &\equiv [b_0\,\Delta t]^{-1} = \frac{\tau_l}{\Delta t} E_0 \,, \end{aligned} \tag{17}$$

where we have used the energy loss term from Eq. (4). We see that while the energy loss timescale $\tau_l \gg \Delta t$, we have $E^\star \approx E$. We see also that there is a maximal energy set by the ratio $\tau_l/\Delta t$: in the Thomson approximation, a particle injected with energy $\geq E^{\rm Th}_{\rm max}$ will have already lost all its energy by Δt. We stress that $E_{\rm max} \geq E^{\rm Th}_{\rm max}$ in the general relativistic case (see Sect. 2.4).

It is worth mentioning that as a further consequence of this energy $E^\star$ arising here, the propagation scale λ is no longer set by energy losses, but instead by the injection time Δt. Indeed, in the simplified case of a constant diffusion coefficient K, we would have found $\lambda^2 = 4\,K\,\Delta t$. Of course, the energy dependence of the diffusion coefficient slightly modifies this relation, but this remark will further help to make a rough prediction of the observed spectrum for a bursting source (see Sect. 2.3).

Finally, we stress that solutions to the time-dependent transport equation do not guarantee causality, which is important to account for to avoid irrelevant predictions when playing with the source age and distance. To ensure causality at zeroth order and for the sake of definitiveness, we will use

$$\begin{aligned} \mathcal{G}_t(t, E, \boldsymbol{x} \leftarrow t_s, E_s, \boldsymbol{x}_s) \;=\; & \theta(c\Delta t - ||\boldsymbol{x} - \boldsymbol{x}_s||)\,\delta(E_s - E^\star) \\ & \times b(E^\star)\,\mathcal{G}(E, \boldsymbol{x} \leftarrow E_s, \boldsymbol{x}_s) \,, \end{aligned} \tag{18}$$

as our time-dependent propagator. A more accurate causal solution would need more specific methods inferred from *e.g.* more detailed studies of the relativistic heat conduction.

2.3. Approximated links between propagation models and observed spectra

To anticipate the discussion on the observed versus predicted spectra primary and secondary electrons, it is useful to show how observed indices can be formally linked to the propagation ingredients. In this section, we establish approximate relations between the observed spectral index $\widetilde{\gamma}$, the source spectral index γ and the propagation parameters. In the most general case, the interstellar (IS) flux at the Earth, *i.e.* without accounting for solar modulation, is expressed as

$$\begin{aligned} \phi_\odot(E) = & \frac{\beta\,c}{4\,\pi} \\ & \times \iiint dt_s dE_s d^3\boldsymbol{x}_s\, \mathcal{G}(E, \boldsymbol{x}_\odot \leftarrow t_s, E_s, \boldsymbol{x}_s)\, \mathcal{Q}(t_s, E_s, \boldsymbol{x}_s) \,. \end{aligned} \tag{19}$$

We will first discuss the steady-state case, before going to the case of time-dependent sources.

The energy dependence arising in the electron propagator (see Sect. 2.1) comes from spatial diffusion and energy losses. At high energy, one can assume that the propagation scale is short enough to neglect the vertical boundary condition, so that one can make use of the 3D propagator to predict the electron flux on Earth, given a source $\mathcal{Q}(E, \boldsymbol{x})$. Since we consider a short propagation scale, and since sources are located in the Galactic disk, we can assume a source term that is homogeneously distributed in the disk. This is a very good approximation for secondaries (see Sect. 3), and fair enough for primaries (see Sect. 4.2). Likewise, let us consider that the source spectrum is a mere power law of index γ, so that the source term can be written as $\mathcal{Q}(E, \boldsymbol{x}) = 2\,h\,\mathcal{Q}_0\,\delta(z)\,\epsilon^{-\gamma}$, where h is the half-height of the disk and ϵ, which is defined in Eq. (4), is the dimensionless energy parameter. Given this source term, the flux on Earth is merely given by:

$$\phi_\odot(E) \;\simeq\; \frac{o\,c\,h}{2\,\pi^{3/2}}\,\frac{\mathcal{Q}_0}{\sqrt{K_0\,b_0}}\epsilon^{-\widetilde{\gamma}} \,. \tag{20}$$

Here, $o = \sqrt{\alpha - \delta - 1}/(\gamma - 1) = \mathcal{O}(1)$, and we have used the 3D propagator defined in Eq. (2), the energy dependence of which is fully determined from Eqs. (3) and (4). Accordingly, the spectral index $\widetilde{\gamma}$ after propagation reads:

$$\widetilde{\gamma} = \gamma + \frac{1}{2}(\alpha + \delta - 1) \,. \tag{21}$$

As it will be discussed in Sect. 2.4, the energy loss rate is dominated by inverse Compton and synchrotron processes. In the non-relativistic Thomson approximation, we have $\alpha = 2$, leading to $\widetilde{\gamma} = \gamma + \frac{1}{2}(1 + \delta)$. From this basic calculation, it is easy to derive rough values for γ and δ consistent with any spectral index $\widetilde{\gamma}$ measured on Earth. For instance, $\widetilde{\gamma} \approx 3$ translates into a source index γ ranging in $[2.1, 2.35]$ for $\delta \in [0.3, 0.8]$. Although very useful at first order, we stress that this crude spectral analysis is only valid for a smooth and flat distribution of source(s), and will in fact significantly differ when considering local discrete effects. Moreover, implementing full relativistic losses induces $\alpha = \alpha_{\rm eff} \lesssim 2$, which implies a harder $\widetilde{\gamma}$. This will be delved into more details in Sect. 4.

Finally, it is also interesting to extract the observed spectral index $\widetilde{\gamma}_\star$ due to a single event-like source, which slightly differs from the above calculation. The source term can be expressed as $\mathcal{Q}_\star = Q_{\star,0}\delta(|\boldsymbol{x}_s| - d)\,\delta(t_s - t_\star)\,\epsilon^{-\gamma}$. Assuming further that the source is located within the propagation horizon $d \ll \lambda$ and bursted at a time much lower than the energy loss timescale $t_\star \ll \tau_l$, the result is readily found:

$$\phi_\odot(E) = \frac{\beta\,c}{4\pi}\,\frac{b(E^\star)}{b(E)}\,\frac{Q_{\star,0}\,\epsilon_\star^{-\gamma}}{(\pi\lambda^2)^{3/2}} \simeq \frac{c}{4\pi}\,\frac{Q_{\star,0}\,\epsilon^{-\widetilde{\gamma}_\star}}{(4\,\pi\,K_0\,t_\star)^{3/2}} \,, \tag{22}$$

with

$$\widetilde{\gamma}_\star = \gamma + \frac{3}{2}\delta \,. \tag{23}$$

Here, we have considered that the propagation scale was no longer fixed by energy losses, since $t_\star \ll \tau_l$, but instead by $t_\star$ (see the discussion at the end of Sect. 2.2). Note that in this case, since $E_\star \sim E$, the spectral index is not directly affected by the energy losses.

2.4. Full relativistic energy losses

In the GeV-TeV energy range, electrons lose their energy by electromagnetic interactions with the ISRF (inverse Compton scattering) and the magnetic field (synchrotron emission), while Bremsstrahlung, ionization and Coulomb processes with the ISM are negligible. Most of studies have used the Thomson approximation to account for inverse Compton losses, which is valid for an electron Lorentz factor $\gamma_e \lesssim m_e c^2/E_\gamma$, where E_γ is the photon energy (*e.g.* Moskalenko & Strong 1998; Delahaye et al. 2009). This translates to a maximal electron energy of $\sim 1.11\times10^6$ GeV for interactions with CMB ($E_\gamma \simeq 2.35\times10^{-4}$ eV), and of $7.58\times10^4/8.66\times10^2$ GeV for IR / starlight radiation, respectively (with $E_{\gamma,\mathrm{IR}/\star} \simeq 3.45\times10^{-3}/0.3$ eV). From those numbers, it is clear that the Thomson approximation is not valid anymore for energies at Earth above a few tens of GeV, for which a full relativistic description of the term dE/dt in Eq. (1) is consequently necessary. Other studies have already implemented this relativistic treatment over the past few years (*e.g.* Kobayashi et al. 2004; Schlickeiser & Ruppel 2009).

The calculation of inverse Compton scattering of electrons with photons in the relativistic regime has been derived a long time ago in the astrophysical context by Jones (1965). It was subsequently extensively revisited and complemented by Blumenthal & Gould (1970). In the following, we will rely on the latter reference to derive our relativistic version of the inverse Compton energy losses, to which we refer the reader for more details.

We assume relativistic electrons propagating in an isotropic and homogeneous gas of photons, which, moreover, exhibits a blackbody energy distribution. The relevance of these assumptions will be discussed in Sect. 2.5. The electron energy loss rate can be expressed in terms of the energies ϵ and ϵ_1 of a photon before and after the collision, respectively, as follows:

$$-\frac{dE}{dt} = \int d\epsilon \int d\epsilon_1 (\epsilon_1 - \epsilon) \frac{dN_\mathrm{coll}}{dt\, d\epsilon\, d\epsilon_1} \,. \quad (24)$$

The collision rate is given by

$$\frac{dN_\mathrm{coll}}{dt\, d\epsilon\, d\epsilon_1} = \frac{3\,\sigma_\mathrm{T}\,c}{4\,\gamma^2} \frac{dn(\epsilon)/d\epsilon}{\epsilon} \times \left\{1 + 2q\left(\ln q - q + \frac{1}{2}\right) + \frac{(1-q)}{2}\frac{(\Gamma q)^2)}{(1+\Gamma q)}\right\} , \quad (25)$$

where $dn(\epsilon)/d\epsilon$ is the initial photon density in the energy range $d\epsilon$, which, for a blackbody radiation has the form (including the two polarization states)

$$\frac{dn}{d\epsilon} = 2 \times \frac{4\pi\epsilon^2}{(2\pi\hbar c)^3} \left(e^{\epsilon/(k_b T)} - 1\right)^{-1} \,, \quad (26)$$

and

$$q \equiv \frac{\hat{\epsilon}_1}{\Gamma(1-\hat{\epsilon}_1)} \;;\; \hat{\epsilon}_1 \equiv \frac{\epsilon_1}{\gamma m c^2} \;;\; \Gamma \equiv \frac{4\gamma\epsilon}{mc^2} \,. \quad (27)$$

From kinematics, the range for $\hat{\epsilon}_1$ is readily found to be $[\hat{\epsilon}, \frac{\Gamma}{(1+\Gamma)}]$, which translates to $[\frac{1}{4\gamma^2}, 1]$ for q. It proves convenient to rewrite the energy loss rate in terms of an integral over q:

$$-\frac{dE}{dt} = \int d\epsilon \int dq \frac{\Gamma^2(\gamma m c^2)^2}{(1+\Gamma q)^2} \cdot \left\{\frac{q}{(1-\Gamma q)} - \frac{1}{4\gamma^2}\right\} \times \times \frac{dN_\mathrm{coll}}{dt\, d\epsilon\, d\epsilon_1} \quad (28)$$

It turns out that the integral over q is analytical, so that one can easily check the full numerical calculation.

Let us define a dimensionless parameter that characterizes the relevant regime to be used for the energy loss rate:

$$\alpha \equiv \frac{\gamma\,(k_b T_0)}{m_e c^2} \,, \quad (29)$$

where T_0 is the mean temperature of the radiation field.

The non-relativistic Thomson limit is recovered for inverse Compton processes within a blackbody radiation field, using $\Gamma \ll 1$ or equivalently $\alpha \ll 1$:

$$-\frac{dE}{dt} = \frac{4}{3}\sigma_\mathrm{T}\, c\, U_\mathrm{rad}\, \gamma^2 \,, \quad (30)$$

where $U_\mathrm{rad} = \int d\epsilon\, \epsilon\, dn/d\epsilon$, whereas the Klein-Nishina regime applies for $\alpha \gg 1$:

$$-\frac{dE}{dt} = \frac{\sigma_\mathrm{T}}{16}\frac{(m_e c\, k_b T_0)^2}{\hbar^3}\left\{\ln\frac{4\gamma\, k_b T_0}{m_e c^2} - 1.9805\right\} \quad (31)$$

In Fig. 1, we show the comparison of both regimes with the full calculation. From our numerical results, we have derived a parameterization valid for any blackbody radiation field, which is given by:

$$-\frac{dE}{dt} = \begin{cases} \mathrm{Thomson} & \text{for } \mathcal{C}_\mathrm{n-r} \\ \frac{E^2 (k_b T_0)^4}{\alpha} \exp\left\{\sum_{i=0} c_i\, (\ln\alpha)^i\right\} & \text{for } \mathcal{C}_\mathrm{int} \\ \mathrm{Klein-Nishina} & \text{for } \mathcal{C}_\mathrm{u-r} \end{cases} \quad (32)$$

where the conditions $\mathcal{C}$ read:

$$\begin{aligned} \mathcal{C}_\mathrm{n-r} &: \alpha < 3.8\times10^{-4} \\ \mathcal{C}_\mathrm{int} &: 3.8\times10^{-4} \leq \alpha \leq 1.8\times10^3 \\ \mathcal{C}_\mathrm{u-r} &: \alpha > 1.8\times10^3 \end{aligned} \quad (33)$$

The fitting formula associated with the intermediate regime and provided in Eq. (32) may be used with the following parameters:

$$c_i = \Big\{74.77, -0.1953, -9.97\times10^{-2}, 4.352\times10^{-3}, 3.546\times10^{-4}, -3.01\times10^{-5}\Big\} \,. \quad (34)$$

An additional smooth interpolation between these three regimes might improve the calculation by avoiding tiny gaps at connections, which could arise *e.g.* from very small numerical differences in the unit conversions or constants used above. This parameterization is valid for any blackbody distribution of photons. If one considers a blackbody distribution, the absolute energy density U_rad of which differs from that standardly derived $U_\mathrm{rad}^\mathrm{bb}$, then one can merely renormalize Eq. (32) by a factor $U_\mathrm{rad}/U_\mathrm{rad}^\mathrm{bb}$ to get the correct energy loss rate.

In the following, we will use Eq. (32) to describe the energy loss rates associated with Compton processes.

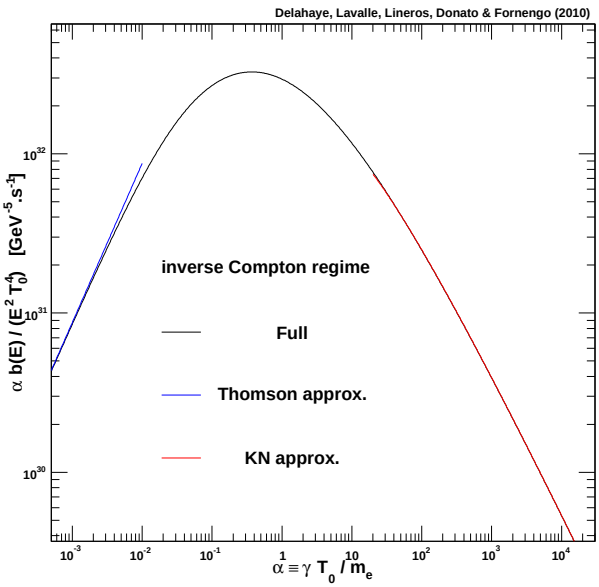

Fig. 1. Comparison between the different relevant regimes of the inverse Compton energy loss for any blackbody radiation field.

2.5. Review of the propagation parameters

On top of energy losses, five parameters regulate the diffusion properties of Galactic CRs: K_0 and δ for the diffusion coefficient (see Eq. 4), the half-thickness of the diffusion zone L, the convective wind velocity V_c, and the Alfvèn speed of magnetic field inhomogeneities V_a, responsible for reacceleration. It was shown in Delahaye et al. (2009) that the last two effects can be neglected above a few GeV. These parameters were self-consistently constrained in Maurin et al. (2001) with ratios of secondary to primary nuclei — mostly boron to carbon B/C (see also Putze et al. 2010, for a more recent analysis). In the following, we will use the available parameter space provided by these authors. Nevertheless, as useful beacons to further discuss or bracket the theoretical uncertainties, we will also use the *min*, *med*, and *max* subsets of propagation parameters, which were derived in Donato et al. (2004) and called so after the hierarchy found on the primary antiproton fluxes, for sources spread all over the diffusion zone (not only in the disk). These models are recalled in Tab. 1.

As regards the normalization of the diffusion coefficient K_0, it is worth noting that B/C measurements actually constrain K_0/L, not K_0 alone (Maurin et al. 2001). Moreover, using radioactive species does not allow yet to fully break this degeneracy (Donato et al. 2002). This explains why the *min* (*max*) configuration, which has a small (large) L, is associated with a small (large) value of K_0. The spectral index of the diffusion coefficient δ decreases from *min* to *max*, which will have importance in the spectral analysis of the electron flux.

Better constraints are expected in the future with next PAMELA data, and hopefully AMS2 (Battiston 2007). The current uncertainty on those parameters leads to large theoretical errors on secondary positrons (Delahaye et al. 2009)

Model	δ	K_0 [kpc^2/Myr]	L [kpc]	V_c [km/s]	V_a [km/s]
min	0.85	0.0016	1	13.5	22.4
med	0.70	0.0112	4	12	52.9
max	0.46	0.0765	15	5	117.6

Table 1. Beacon sets of diffusion parameters derived in Donato et al. (2004) and compatible with the B/C analysis performed in Maurin et al. (2001). The *med* setup will be our default model.

and therefore electrons, as it will be reviewed in Sect. 3. The error on astrophysical primaries will be studied in Sect. 4.4

At variance with stable nuclei in the GeV-TeV energy range, electrons strongly suffer energy losses, which turn out to be of the most important processes affecting their transport. It was shown in Delahaye et al. (2009) that only inverse Compton and synchrotron processes were significant in this energy domain. Therefore, it is crucial to constrain the ISRF — including the CMB, and radiations from dust and stars — and the magnetic field as accurately as possible, within the horizon of GeV-TeV electrons, *i.e.* $\mathcal{O}(1\,\mathrm{kpc})$.

In Sect. 2.4, we have developed a method to treat inverse Compton processes in a full relativistic formalism, provided the target radiation fields can be described in terms of black-body distributions. This is obviously the case for the CMB, the temperature of which was recently reestimated in Fixsen (2009) to 2.7260±0.0013 K. However, it is well known that the ISRF is not a simple Planckian radiation, since it involves many different components — IR radiation from dust, optical and UV radiation from stars, diffuse X-ray emission, *etc.* — with different spatial distributions. Since from CMB only we can estimate the electron propagation scale to be $\lesssim 2$ kpc for electron energies above 10 GeV, we can still safely disregard the spatial dependence, and only consider local averages.

In the left panel of Fig. 2, we report the ISRF data that we extracted from the analysis made in Porter et al. (2008), and that we averaged in boxes of 500×500 pc and 2×2 kpc around the Earth, on top of which we show that a sum of black-body distributions can actually provide a reasonable fit. These two models, defined with a set of components characterized by their temperatures and energy densities, are summarized in Tab. 2. They can be used to size the theoretical error coming from uncertainties in the characterization of ISRF. We can hope that these uncertainties somehow reflect those affecting the data that we used, and which are not available. Note that the parameterizations appearing in Tab. 2 are not aimed at reflecting the actual radiative physics at stake in the ISM, which is beyond the scope of this paper. Nevertheless we still observe an interplay between the IR and UV components, depending on the averaging volume: a smaller volume gives a larger (smaller) IR (UV) contribution, due to the efficient UV-absorption and IR-emission properties of the dust mostly concentrated in the disk.

The synchrotron emission can also be expressed as an inverse Compton scattering on a black-body distribution of virtual photons from the magnetic field. In this case, the characteristic energy of the radiation field is given by the

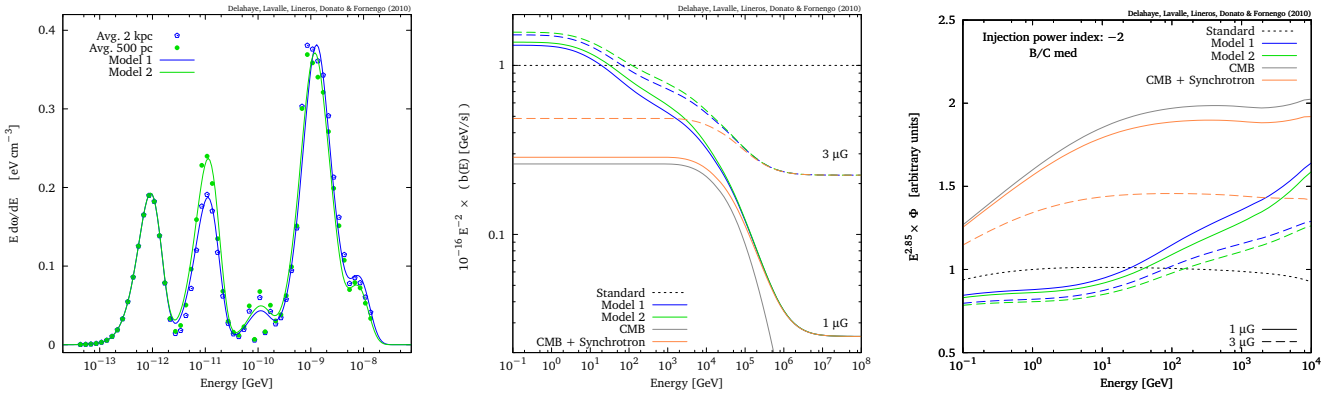

Fig. 2. Left: Energy density distribution of the ISRF averaged in 2 boxes of different volumes, where all components appear (data taken from the analysis by Porter et al. (2008)). Our models 1 and 2, using both black bodies for all components, are reported against the data. Middle: Corresponding energy loss rate. Right: Toy electron fluxes associated with the previous energy loss configurations, assuming an injection spectrum $\propto E^{-2}$.

		T_0[K]	U_{rad} [GeV.cm^{-3}]
	CMB	2.725	Planckian
M1	IR	33.07	9.40 10^{-11}
	Stellar	313.32	2.0210^{-11}
	UV	3 249.3	1.37 10^{-10}
		6 150.4	8.4810^{-11}
		23 209.0	4.40 10^{-11}
M2	IR	33.653	1.19 10^{-10}
	Stellar	313.32	2.2910^{-11}
	UV	2 901.13	1.25 10^{-10}
		5 570.1	9.60 10^{-11}
		22 048.56	3.8 10^{-11}

Table 2. Parameters used to fit the local ISRF with blackbodies. M1 and M2 correspond to fits done on the data taken from the analysis made in Porter et al. (2008) averaged over 2 × 2 kpc and 0.5 × 0.5 kpc around the Earth, respectively. M1 will be our default ISRF model.

cyclotron frequency:

$$E_B = h\,\nu_c = \frac{h\,e\,B}{2\,\pi\,m} = 1.16\times10^{-14}\left[\frac{B}{1\,\mu\mathrm{G}}\right]\ \mathrm{eV}\ , \qquad (35)$$

where m is the electron mass, k_B is Boltzmann's constant and B is the value of the Galactic magnetic field. It is clear that the condition $\gamma\,E_B \ll m\,c^2$ is fulfilled for the whole electron energy range considered in this paper, so that the Thomson approximation is fully valid. The local magnetic field is estimated to $B \approx 1\mu$G (Ferrière 2001) while the corresponding energy density derived from classical electrodynamics is $U_B = B^2/(2\mu_0)$.

Although there are uncertainties on the local value of the magnetic field, we will fix $B = 1\,\mu$G in the following, so that the ISRF model M1 plus synchrotron leads to $\tau_l = 7.5\times10^{15}$ s in the Thomson approximation. The corresponding overall energy loss rate $b(E)/E^2$ is plotted in the middle panel of Fig. 2, where it is shown to be quite different from the Thomson approximation with $\tau_l = \mathrm{cst} = 10^{16}$ s very often used in the literature, and which appears as the dashed straight line. In particular, we can observe a cascade transition due to Klein-Nishina effects, where we see that the loss rate index α defined in Eq. (4) decreases step by step from 2, its Thomson value: at about 1 GeV, relativistic corrections become sizable for interactions with the main UV component which is less and less felt by electrons; then, between 10-100 GeV the IR component gradually loses its braking potential, and finally, above 10 TeV, interactions with CMB also ceases. The value of the magnetic field sets the minimal value of the energy loss rate at higher energies. Since this latter is proportional to B^2, varying B from 1 to 3 μG translates into ~ 1 additional order of magnitude in the energy loss rate at high energy, as also depicted in the middle panel of Fig. 2. Note that considering CMB only provides a robust estimate of the minimal energy loss rate, which converts into a maximal flux by virtue of Eq. (20); adding the synchrotron losses would instead define a next-to-minimal model for the energy losses.

In the right panel of Fig. 2, we quantify the impact of using different energy loss models to derive IS flux predictions, for which we adopt the *med* propagation setup and a template injection spectrum $\propto E^{-2}$ homogeneously distributed in a thin disk. The dotted curve corresponds to the Thomson approximation with $\tau_l = 10^{16}$s, where we recover a flux with predicted index $\widetilde{\gamma} = \gamma + (\delta+1)/2 = 2.85$, as predicted from Eq. (21) with $\alpha = 2$. The higher curve is the flux obtained with the minimal case for the energy loss rate (the minimal τ_l), *i.e.* considering the CMB only, which provides the maximal flux. Indeed, in the Thomson approximation, the flux scales like $\sim\sqrt{\tau_l} = 1/\sqrt{b_0}$, as seen from Eq. (20). Again, the index reaches a plateau around $\widetilde{\gamma}\approx 2.85$ in the range 10-1000 GeV, and then substantially hardens above 1 TeV because of relativistic effects. The next-to-minimal case exhibits the same feature, though the amplitude is slightly reduced, as expected. Finally, we report the flux associated our complete models M1 and M2, both associated with a magnetic field of 1 (solid curves) or 3 μG (dashed curves). We can remark that the naive prediction of $\widetilde{\gamma}$ in the Thomson regime does not hold anymore, since the energy dependence of the energy loss α is no longer equal to 2, and the observed spectral index is actually significantly harder. Indeed, we have to consider instead an effective value $\alpha_{\rm eff}(E) \lesssim 2$ to account for relativistic effects. Taking a larger value of the magnetic field slightly softens the index and increases the amplitude, as expected.

From this analysis of the local energy losses, we can estimate that the related uncertainties translate into a factor of $\lesssim 2$ in terms of IS flux amplitude ($\phi \propto \sqrt{\tau_l}$), and, above 10 GeV, ± 0.1 in terms of spectral index — see the left panel of Fig. 2. Notice, however, that this crude spectral analysis is valid for a smooth distribution of sources only, *i.e.* for secondaries. We will see in Sect. 4.3 that considering discrete nearby sources of primaries strongly modifies this simplistic view.

3. Secondary CR electrons and positrons

We have already performed an exhaustive study of the secondary positron flux in Delahaye et al. (2009), which is qualitatively fully valid for electrons and to which we refer the reader for more details.

Secondary electrons originate from the spallation of hadronic cosmic ray species (mainly protons and α particles) on the interstellar material (hydrogen and helium). This process produces electrons and positrons as well, except, of course, that different inclusive cross sections come into play. Since spallation involves positively charged particles, charge conservation implies that spallation creates more positrons than electrons (*e.g.* Kamae et al. 2006). This statement is slightly alleviated when considering neutron decay, but electrons arising from neutron decay have a very low energy (mostly E < 10 MeV), thereby out of the energy range considered in this paper. Anyway, the steady-state source term for secondaries may be written as

$$\mathcal{Q}_s(E,\boldsymbol{x}) = 4\pi \sum_{i,j} \int dE'\, \phi_i(E',\boldsymbol{x})\, \frac{d\sigma_{ij}(E',E)}{dE}\, n_j(\boldsymbol{x})\ , \quad (36)$$

where i flags the CR species of flux ϕ and j the ISM gas species of density n, the latter being concentrated within the thin Galactic disk. $d\sigma_{ij}(E',E)$ is the inclusive cross section for a CR-atom interaction to produce an electron or positron of energy E.

For our default computation we have selected the proton-proton cross section parameterizations provided in Kamae et al. (2006). Any nucleus-nucleus cross section (*e.g.* p-He or He-He) can be derived from the latter by applying an empirical rescaling, usually by means of a combination of the involved atomic numbers. Note, however, that this rescaling is found different for the production of π^- and π^-, or equivalently of e^- and e^+. We have used the prescriptions from Norbury & Townsend (2007) for this empirical rescaling.

Fits of the proton and α particles fluxes are provided in Shikaze et al. (2007), based on various measurements at the Earth. Finally, we have employed a constant density for the ISM gas, with $n_H = 0.9\,\mathrm{cm}^{-3}$ and $n_{He} = 0.1\,\mathrm{cm}^{-3}$, confining these species into a thin disk of half-height $h = 100$ pc. This is summarized in cylindrical coordinates by:

$$n_j(\boldsymbol{x}) = \theta(h - |z|)\,\theta(R - r)\,n_j\ . \quad (37)$$

With such a spatial distribution for the gas, the spatial integral of Eq. (19) can be calculated analytically, following Delahaye et al. (2009); the solution is reported in Sect. A.1. We stress that this approximation is locally rather good over the whole energy range as long as the actual gas distribution does not exhibit too strong spatial gradients over a distance set by the half-thickness L — this will be discussed in more details for primaries in Sect. 4.2. In any case, it is good at high energies ($\gtrsim 100$ GeV) for which the signal is of local origin whatever L. At lower energies such an approximation is actually fair for moderate $L \lesssim 4$ kpc, but our low energy predictions for secondaries might be less trustworthy for the *max* propagation setup. To treat such extreme configurations more accurately, a better description of the gas distribution would be necessary.

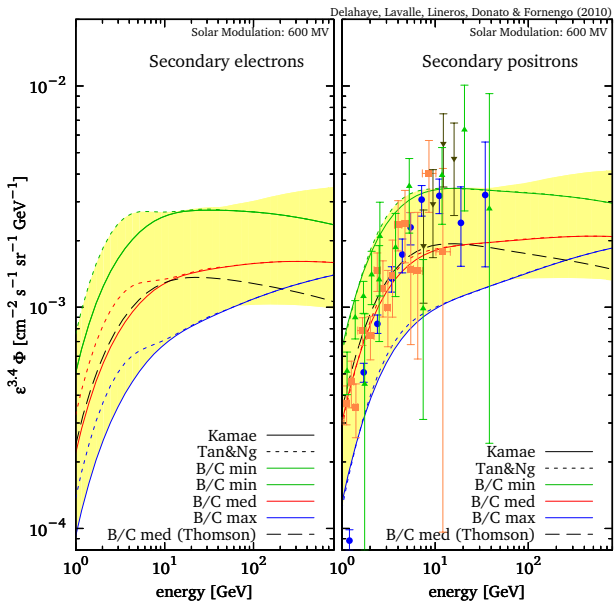

Fig. 3. Flux predictions of secondary electrons (left) and positrons (right) at the Earth, for the *min*, *med* and *max* propagation setups.

In Fig. 3, we plot our results for the secondary electron (left hand side) and positron (right hand side) fluxes at the Earth. For the solar modulation, we have used the force-field approximation with a Fisk potential of 600 MV (Fisk 1971). The solid curves are derived with the M1 ISRF model, a relativistic treatment of energy losses and nuclear cross sections from Kamae et al. (2006). The yellow band is the flux range available for all sets of propagation parameters compatible with B/C constraints derived in Maurin et al. (2001). We observe that the *min* (*max*) configuration provides the highest (lowest) and softest (hardest) flux, among the three beacon setups. This is actually not surprising if we look at Eq. (20), since the *min* configuration is typified with the weakest value of diffusion coefficient normalization K_0 associated with the strongest index δ, which is reversed in the *max* configuration. However, we remind that these models were named so for sources distributed all over the diffusion halo, not only confined in the disk as it is the case here.

The discussion made in Delahaye et al. (2009) on the theoretical uncertainties affecting secondary positrons is fully valid for secondary electrons. Aside from energy losses, errors may originate from uncertainties on the light nuclei flux, and from uncertainties on nuclear cross sections. The former can be evaluated by using different fits of the local measurements, and also by retro-propagating the CR nuclei flux to account for potential spatial gradient. The latter may be estimated by considering alternative parameterizations of nuclear cross sections. This is illustrated in Fig. 3 with the short-dashed curves which were computed with

the nuclear cross sections from Tan & Ng (1983), which are shown to differ from our default model only at low energy below a few GeV. All these effects were studied for positrons in Delahaye et al. (2009), which implied an uncertainty of about 40 %; this theoretical error is valid for secondary electrons as well. It is worth mentioning, however, as we will see later, that the electron flux is likely dominated by the primaries, at variance with positrons for which secondaries are a major component. Therefore, uncertainties on the secondary contribution has more impact for positrons than for electrons.

Finally, we stress that the present results are slightly different from those derived in Delahaye et al. (2009) because the energy losses are treated in a full relativistic formalism. Not only does this slightly change the normalization at low energy by a factor $\sqrt{\tau_l/\tau_{\rm D09}} \approx 0.9$, but, more important, this hardens the spectral shape due to Klein-Nishina effects. This is more striking in Fig. 3, where the long-dashed curves are the predictions calculated in the *med* configuration and in the Thomson limit for energy losses. In App. B, we provide user-friendly fitting formulae that fairly well reproduce our calculations of the secondary electron and positron fluxes in the *med* propagation setup.

4. Primary electrons

The GeV-TeV CR electron flux at the Earth is dominated by a primary component originating from those electrons accelerated in SNRs and pulsar wind nebulæ(PWN) (Blandford & Eichler 1987). CR sources are therefore connected to the explosion of supernovæ(SNe), and we will discuss a more general framework in Sect. 5. Predicting this primary contribution is a rather difficult exercise since this implies to characterize the energy distribution of these electrons at sources and their spatial distribution, in addition to their transport to the Earth. Moreover, since GeV-TeV electrons have a short range propagation scale, local sources are expected to play an important role. Rephrased in statistical terms, since the number of sources exhibits large fluctuations at short distance, the variance affecting the predictions is expected to increase with energy, when the propagation volume decreases. Therefore, fluctuations in the properties of local sources will have strong impact. Reversely, the low energy part of the CR electron spectrum might be safely described from an average source properties, namely a smooth spatial distribution associated with a mean injected energy distribution.

In the following, we aim to estimate the primary flux of electrons and at quantifying the associated theoretical errors. More precisely, we wish to quantify the relative origin and impact of these uncertainties. To do so, we will first discuss in Sect. 4.1 the spectral shape properties that we will consider in the forthcoming calculations, focusing on SNRs for the moment (pulsars will be discussed in Sect. 5, together with primary positrons); available spatial distributions will be presented in Sect. 4.2. Then, we will discuss the uncertainties associated with the modeling of a single source in Sect. 4.3. We will finally discuss the primary flux and related uncertainties in Sect. 4.4, in which we will make a thorough census of the local SNRs that likely affect the high energy part of the spectrum.

4.1. Spectral properties of SNRs and related constraints

Most SNR models (*e.g.* Ellison et al. 2007; Tatischeff 2009) rely on the acceleration of CRs at non-relativistic shocks (*e.g.* Malkov & O'C Drury 2001) and predict similar energy distributions for the electrons released in the ISM, which can be summarized as

$$\mathcal{Q}(E) = \mathcal{Q}_0 \epsilon^{-\gamma} \exp\left\{-\frac{E}{E_c}\right\} . \quad (38)$$

The spectral index γ is usually found around 2 over a significant energy range (Ellison et al. 2007) — but exhibiting large variation at the edges — in agreement with radio observations, and gamma-ray observations (*e.g.* Aharonian et al. 2009b) suggest that the energy cut-off E_c is greater than a few TeV. Moreover, these studies find rather similar indices for protons and electrons. Since protons above a few GeV are barely affected by energy losses and have long range propagation scale, the proton spectrum measured at the Earth can provide information on the mean index at sources. Since $\phi_p \propto \mathcal{Q}(E)/K(E) \propto E^{-\widetilde{\gamma}}$, the index at source is therefore $\gamma \approx \widetilde{\gamma} - \delta$. With $\widetilde{\gamma} \simeq 2.8$ and δ ranging in 0.5-0.7, one finds γ ranging in 2.0-2.3, in rough agreement with theoretical predictions. We will discuss complementary constraints coming from radio observations at the end of this subpart.

Aside from the spectral shape, sizing the value of the normalization $\mathcal{Q}_0$ is much more problematic. To describe a distribution of sources in the Galaxy, one usually assumes that the high energy electron injection is connected to the explosion rate of SNe, so that we can guess that Q_0 is such that the total energy carried by electrons:

$$\int_{E_{\rm min}}^{\infty} dE'\, E'\, \mathcal{Q}(E') = f\, E_\star\, \Gamma_\star , \quad (39)$$

where $\Gamma_\star$ is the SN explosion rate, $E_\star$ is the kinetic energy released by the explosion and f is the fraction of this energy conferred to electrons. Since we are interested in the non-thermal electrons only, we will fix $E_{\rm min} = 0.1$ GeV. It is worth mentioning that the spectral index influences the normalization procedure sketched above. For a single source, the same expression holds but without $\Gamma_\star$. We will discuss this case later on. For convenience, we define the following quantities

$$\begin{aligned} \widetilde{E}_\star &\equiv f\, E_\star \quad (40)\\ \widetilde{\Gamma}_E &\equiv \Gamma_\star\, \widetilde{E}_\star , \end{aligned}$$

which will further be helpful to discuss the normalization issue.

The question arises of constraining $\Gamma_\star$, $E_\star$ and f. The explosion rate of SNe is typically predicted to be a 1-5 per century and per galaxy (*e.g.* van den Bergh & Tammann 1991; Madau et al. 1998), which is consistent with observations (*e.g.* Valinia & Marshall 1998; Diehl et al. 2006). Nevertheless, SNe are of different types, and may thereby lead to different CR acceleration processes. About 2/3 of SNe are expected to be core-collapse SNe (CCSNe), the remaining 1/3 being composed of type 1a SNe (SNe1a). This is at variance with the statistics derived from observations, which favors the more luminous latter type. CCSNe arise in star formation regions from the collapse of massive stars $\gtrsim 8\, M_\odot$, while SNe1a, originating from older accreting white dwarves, are more modest systems while more widely distributed.

Explosions of CCSNe with masses $\lesssim 20\,M_\odot$ can liberate a huge amount of energy, 10^{53-54} erg typically, $\sim 10\%$ of which is in the form of neutrinos (*e.g.* Burrows 2000; Woosley & Janka 2005; Janka et al. 2007). They usually lead to quite complex systems characterized by SNRs beside (or inside) which one can find active neutron stars like pulsars and associated wind nebulæ (PWN) — we will focus on pulsars in Sect. 5. Aside, SNe1a are much more modest systems and release about 10^{51} erg of kinetic energy in the ISM (*e.g.* Nomoto et al. 1984; Gamezo et al. 2003; Mazzali et al. 2007). Since we will only deal with SNRs in this part, we will fix $E_\star = 10^{51}$ erg in the following.

The fraction of SN energy conferred to electrons was recently studied in Tatischeff (2009), and found about $f \sim 10^{-5} - 10^{-4}$. This result turns out to be rather independent from the exact values of the spectral index γ and the cut-off energy E_c, but the theoretical error is still of about one order of magnitude.

We emphasize that at this stage, the theoretical uncertainty on $\widetilde{\Gamma}_E = f\,E_\star\,\Gamma_\star$ already reaches about 2-3 orders of magnitude in average, which is quite huge and translates linearly in terms of flux.

For known single sources, it is possible to derive better constraints on the individual normalizations $\mathcal{Q}_0$ from observations in wavelengths for which electrons are the main emitters. This is precisely the case for the non-thermal radio emission due to synchrotron processes, provided the magnetic field is constrained independently. The synchrotron emissivity associated with an electron source of injection rate $\mathcal{Q}(E)$ reads (Ginzburg & Syrovatskii 1965; Blumenthal & Gould 1970; Longair 1994):

$$J(\nu) = \frac{1}{2}\int_0^\pi d\theta\,\sin(\theta)\int d\nu\,P_s(\nu,\theta)\,\mathcal{Q}(E=h\nu)\;, \tag{41}$$

where an average is performed over the pitch angle θ, and where the synchrotron radiation power is defined as:

$$\begin{aligned} P_s(\nu,\theta) &= \frac{\sqrt{3}\,e^3\,B}{4\,\pi\,\epsilon_0\,m\,c}\,x\int_{x/\sin(\theta)}^\infty dy\,K_{5/3}(y) \\ \text{with}\;\; x &\equiv \frac{\nu}{\nu_s}\;;\;\nu_s \equiv \frac{3}{2}\,\gamma^2\,\nu_c = \frac{3\,e\,B\gamma^2}{4\,\pi\,m}\;. \end{aligned} \tag{42}$$

ν_s, which is called the *synchrotron peak frequency*, corresponds to the average frequency of the synchrotron emission arising when an electron of Lorentz factor γ interacts with a magnetic field B, and is $\propto \gamma^2\nu_c$, where ν_c is the cyclotron frequency. Note the parallel with the inverse Compton process for which an initial photon of energy E_k would be boosted to $\sim \gamma^2 E_k$. While we can derive the radio flux from the emissivity, it is a bit more striking to work out a more intuitive expression, which actually turns out to provide a fair approximation (Longair 1994):

$$\frac{d\phi(\nu)}{d\nu}\,d\nu \simeq \frac{[b(E)]_{\rm sync}}{4\,\pi\,d^2\,h\nu}\,\mathcal{Q}(E)\,dE\;. \tag{43}$$

Here, we assume that the entire radiation is emitted at the synchrotron peak frequency $\nu = \nu_s$, which further links ν and E. The distance from the observer to the source is denoted by d. Notice that only the synchrotron part of the electron energy loss rate $b(E)$ appears — we therefore assume that this is the most efficient process within the source — and that we also neglect the possible re-absorption of the synchrotron emission. Since $b(E)$ is the energy lost by an electron, it corresponds to the energy of the emitted photon, so that the factor $1/(h\nu)$ allows to infer the number of photons.

Armed with this expression, we can now constrain $\mathcal{Q}_0$ by means of the source radio brightness $B_r(\nu)$, which is usually found in catalogs:

$$\begin{aligned} B_r(\nu) &= \frac{1}{\delta\nu}\int_\nu^{\nu+\delta\nu} d\nu'\,h\nu'\,\frac{d\phi(\nu')}{d\nu'} \\ &\overset{\delta\nu\to 0}{=} \frac{[b(E)]_{\rm sync}}{4\,\pi\,d^2}\;\mathcal{Q}(E)\,\frac{dE}{d\nu}\;. \end{aligned} \tag{44}$$

We readily derive:

$$\mathcal{Q}_0 = \frac{4\,\pi\,d^2}{[b(E)]_{\rm sync}}\left(\frac{E}{E_0}\right)^\gamma\,\frac{d\nu}{dE}\,B_r(\nu)\;, \tag{45}$$

which translates to

$$\begin{aligned} \frac{\mathcal{Q}_0}{\rm GeV^{-1}} &= 1.2\times 10^{47}\times(0.79)^\gamma \\ &\times\left[\frac{d}{\rm kpc}\right]^2\left[\frac{\nu}{\rm GHz}\right]^{\frac{\gamma-1}{2}}\left[\frac{B}{100\,\mu\rm G}\right]^{-\frac{(\gamma+1)}{2}}\left[\frac{B_r(\nu)}{\rm Jy}\right]\;. \end{aligned} \tag{46}$$

Note that we have recovered the well-known relation between the radio index and the electron index, $\gamma_r = (\gamma-1)/2$.

An up-to-date catalog of SNRs can be found in Green (2009), which contains ∼265 objects. Among these objects, only 70 have estimated distances to the Earth has, and 207 have measured radio spectral indices. Observations, however, are not expected to reflect the actual statistical properties of the whole population of Galactic SNRs because of observational selection effects favoring the brightest sources as well as sites of fainter background (high longitudes, towards the anticenter). Anyway, disregarding the spatial distribution of these objects which is likely strongly biased, such a sample may still be fairly representative of their general spectral properties (Green 2005).

We have made histograms of the measured radio indices and of the estimated intrinsic luminosities — $\mathcal{L}/(4\,\pi) = d^2\,B_r(1\,\rm GHz)$ — in the right and left panels, respectively, of Fig. 4. It clearly appears that the radio indices exhibit a Gaussian distribution, whereas luminosities follow a log-normal distribution. This points towards similar physical grounds for the electron properties at sources, which is obviously not surprising. With these distributions, we can derive mean values and statistical ranges for the parameters. We find $\langle\gamma_r\rangle = 0.50\pm0.15$ and $\langle d^2\,B_r(1\,\rm GHz)\rangle = \exp\{6.26\pm1.95\}$ Jy.kpc^2. One can therefore infer the electron index $\langle\gamma\rangle = 2\,\langle\gamma_r\rangle + 1 = 2.0\pm0.3$ in very good agreement with theoretical expectations. Although this relation between the radio index and the electron index is not completely exact (other radio components, absorption), and although some systematic errors also affect the data, this provides a complementary mean to bracket the uncertainty, which is consistent with theoretical results.

We can use this statistical information to constrain directly the single source normalization $\mathcal{Q}_0$ from Eq. (46), but we further need an estimate of the magnetic field in SNRs. From the observational point of view, information on electron density and magnetic field at sources is degenerate. More insights may come from theoretical studies on the amplification of magnetic fields in sources from numerical simulations, which involve CRs themselves as seeds and amplifiers. The current state-of-the-art (*e.g.* Lucek & Bell

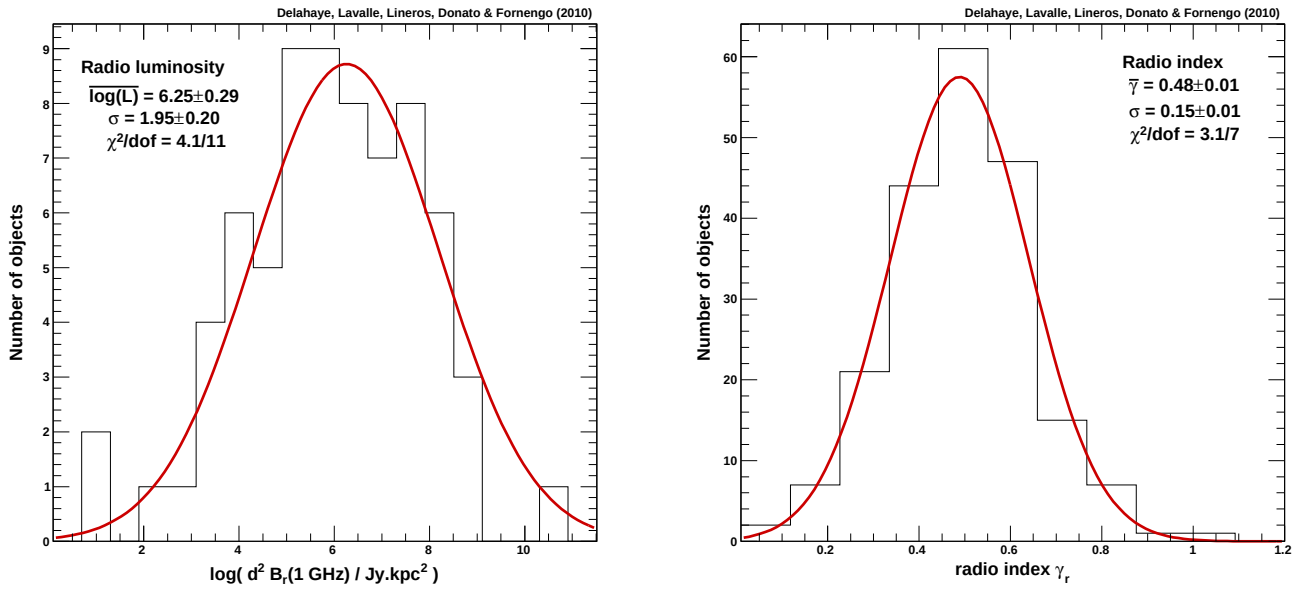

Fig. 4. Left: histogram of SNR luminosities — $\mathcal{L}/(4\,\pi) = d^2\,B(1\,\mathrm{GHz})$. Right: histogram of SNR radio spectral indices. The SNR data are taken from the Green catalogue (Green 2009).

2000) gives $B \sim 100\,\mu$G, in agreement with observations, and that we will further use. With this value, we finally find $\langle \mathcal{Q}_0 \rangle = 3.9 \times 10^{49}\,\mathrm{GeV}^{-1}$ for an index $\gamma = 2$, which translates into $\langle \widetilde{E}_\star \rangle \simeq 4.3 \times 10^{50}\,\mathrm{GeV} \simeq 6.9 \times 10^{47}\,\mathrm{erg}$ (with a cut-off $E_c = 10$ TeV). This is in rough agreement with the other values derived above, but probably biased, as expected, towards the brightest objects.

4.2. Spatial distribution of sources

Although GeV-TeV electrons have a short range propagation scale, the injection rate of energy discussed above is not sufficient to describe the Galactic CR electrons. We further need to specify the spatial distribution of sources. For nearby sources, we can use available catalogs since observational biased are less prominent, so that they may provide a rather good description of the local injection. Nevertheless, for more distant sources, which will have influence in the intermediate energy range ∼1-100 GeV, we have to rely on a distribution model.

Since 2/3 of SNe are expected to be CCSNe, one can use pulsars as tracers of the SNR distribution, instead of SNRs themselves whose observed population is much more modest. Indeed, as an illustration, the ATNF catalog[2] (Manchester et al. 2005) lists more than 1800 pulsars compared to the ∼265 SNRs contained in Green (2009). Nevertheless, a too naive use of the statistics would lead to errors since it is well known that data do not reflect reality faithfully because of detection biases (*e.g.* Lorimer 2004).

There are few distribution models in the literature that we can compare. Since the energetics associated with the source injection (birth) rate has been discussed above, we are only interested in the *normalized* source distribution. Consequently, the normalization coefficient in front of each model will be fixed such that it normalizes the spatial distribution within the diffusion halo characterized by its radius R and half-thickness L. Moreover, in the following, we will set the position of the Sun at $R_\odot = 8$ kpc from the Galactic center[3].

Most of models exhibit radial and vertical dependencies in the form

$$\rho(r,z) = \rho_0\, r^a\, \exp\left\{-\frac{r}{r_0}\right\}\, \exp\left\{-\frac{|z|}{z_0}\right\}\ , \qquad (47)$$

where ρ_0 ensures the normalization to unity. For simplicity, we will only discuss differences in the radial distributions in the following, since the vertical distribution is rather consensual among studies. Consequently, we will keep fixed the vertical dependency like in the above equation, with $z_0 = h = 0.1$ kpc, throughout the paper.

Different sets of values can be found in the literature for the pair (a, r_0). Lorimer (2004), hereafter L04, found $(2.35, 1.528\,\mathrm{kpc})$; Yusifov & Küçük (2004), hereafter YK04, derived $(4, 1.25\,\mathrm{kpc})$; while Paczynski (1990), hereafter P90, early determined $(1, 4.5\,\mathrm{kpc})$. Finally, at variance with the parameterization sketched above, let us mention the distribution proposed by Case & Bhattacharya (1998), hereafter CB98, though it was obtained from a fit on a poor statistics of 36 SNRs:

$$\rho(r,z) = \rho_0\, \sin\left(\pi\frac{r}{r_s} + \theta\right)\, \exp\left\{-\frac{r}{r_0}\right\}\, \exp\left\{-\frac{|z|}{z_0}\right\}\ , \qquad (48)$$

where we have added the same vertical term as in Eq. (47). The authors found $r_0 = 7.7 \pm 4.7$ kpc, $r_s = 17.2 \pm 1.9$ kpc and $\theta = 0.08 \pm 0.33$. This relation is only valid for $r < r_s(1 - \theta/\pi)$, *i.e.* within 16.8 kpc, and null beyond. Note however that Brogan et al. (2006) recently reported

[2] `http://www.atnf.csiro.au/research/pulsar/psrcat`

[3] Some of the distributions listed in this paragraph are actually derived assuming 8.5 kpc, but we will disregard this small change to make the discussion easier.

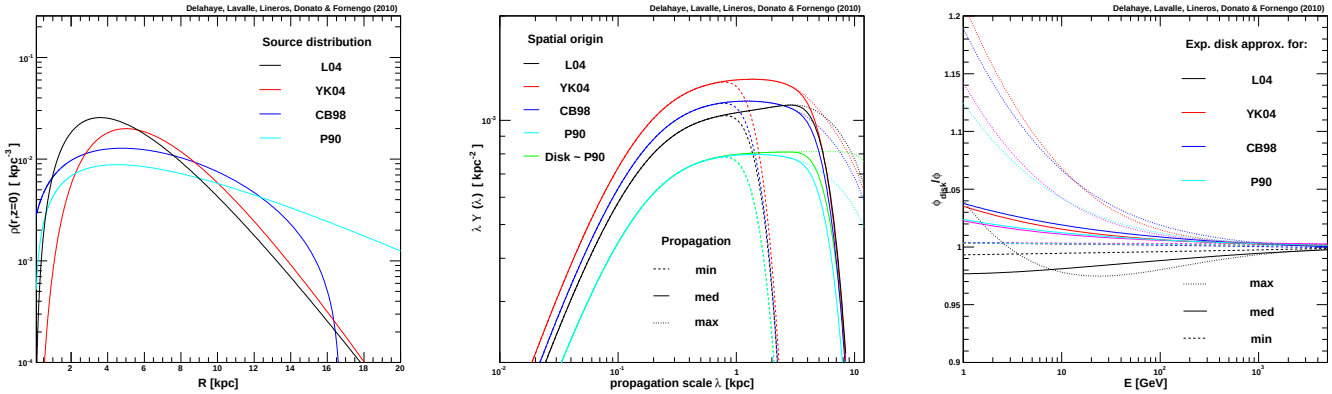

Fig. 5. Left: Spatial distribution models for SNRs and pulsars. Middle: Corresponding halo functions defined in Eq. (49) and that size the transport probability as a function of the propagation scale λ, which decreases with energy. Right: Ratio of flux predictions to their associated exponential disk approximations.

the detection of 35 new remnants in the inner Galaxy, and suggest that former radial distribution estimations should be revised.

In order to understand the deviations induced in the electron flux prediction when using these different distributions, it is convenient to define the following *halo function*

$$\Upsilon_\odot(\lambda) = \int d^3\boldsymbol{x}_s \, \rho(r_s, z_s) \, \mathcal{G}_\lambda(\lambda, \boldsymbol{x}_\odot \leftarrow \boldsymbol{x}_s) \qquad (49)$$

$$\text{where} \quad \mathcal{G}_\lambda(\lambda, \boldsymbol{x}_\odot \leftarrow \boldsymbol{x}_s) \equiv b(E) \, \mathcal{G}(E, \boldsymbol{x}_\odot \leftarrow E_s, \boldsymbol{x}_s) \ ,$$

which sizes the probability for an electron to reach the Earth given its propagation scale λ — see Eq. (3) — and the normalized spatial distribution of source ρ. The electron flux is merely the energy integral of this probability times the source spectrum, so that the shape of this probability function gives a preliminary taste of the final result. More important, it allows to connect the spatial origin of the signal with energy, through the propagation scale λ.

In the left panel of Fig. 5, we plot the spatial distribution listed above as a function of the galactocentric radius r, and in the galactic plane $z = 0$. We see that except in the solar neighborhood, where relative amplitudes can vary by a factor of $\sim$2 at maximum, they are quite different in the direction of the Galactic center as well as towards the anticenter. Nevertheless, these differences are significantly smoothened when calculating $\Upsilon_\odot(\lambda)$, because of the spatial average — see Eq. (49). This is shown in the middle panel of Fig. 5, where we have plotted $\lambda \times \Upsilon_\odot(\lambda)$ as a function of λ for the different spatial distributions and for the *min*, *med* and *max* propagation setups. We see that the probability is maximal and constant — $\lambda\,\Upsilon_\odot$ grows linearly with λ — for short propagation scales up to $\lambda \sim h = 0.1$ kpc. Then, the probability decreases linearly with λ — $\lambda\,\Upsilon$ exhibits a plateau — before shrinking exponentially when $\lambda \sim L$, which naturally occurs farther and farther when going from *min* to *max*. Notice that each spatial distribution model is characterized by a very similar curve that mostly differs in terms of amplitude. This can be understood in the following manner: when $\lambda < h$, the source can be considered as homogeneous in 3D space, then $\Upsilon_\odot \propto \int dr\, r^2 \lambda^{-3} \exp\{-r^2/\lambda^2\} = \text{cst}$; when $h < \lambda < L$, since the source distributions do not exhibit strong radial variations at the kpc scale, they can be considered as thin disks, and one recover the solution $\Upsilon \propto \lambda^{-1}$ derived in Eq. (20); for $\lambda > L$, electrons escape the diffusion zone. This points towards the possibility of modeling, while only locally, the source distribution with a z-exponential infinite disk, for which full analytical solutions of the spatial integral exist. The green curve in the middle panel of Fig. 5 is the z-exponential disk approximation associated with P90, as an illustration, and is shown to provide a rather good approximation except for large diffusion thickness $L \gtrsim 4$ kpc. The z-exponential disk approximation is defined in cylindrical coordinates as:

$$\rho_d(r, z) = \rho(R_\odot, 0) \, \theta(R - r) \, \exp\left\{-\frac{|z|}{z_0}\right\} \ , \qquad (50)$$

where $\rho(R_\odot, 0)$ is the local value of the normalized density given in Eq. (47). This approximation is valid for local predictions provided the spatial distribution ρ does not vary significantly over a distance $\sim L$, which is the case for moderate L. In the right hand side panel of Fig. 5, we compare the disk approximation with the full calculation in terms of fluxes: for different spatial distributions, we plot the ratio *approximated flux / exact flux* for our three beacon propagation setups. We can see that the exponential disk approximation is quite good above a few GeV for the *min* and *med* cases, as expected, with an accuracy better than 5%. Errors are obviously larger for the *max* case because of the larger spatial gradients exhibited by the spatial distributions within $L = 15$ kpc.

A final useful exercise regarding the smooth spatial distribution modeling consists in checking the cumulative fraction of the IS signal received at the Earth as a function of the radial integration distance. In Fig. 6, we plot this fraction for spatial model L04 at different energies, assuming an injection spectrum $\propto E^{-2}$, and for both the Thomson approximation and the relativistic energy losses. We see that this fraction increases more quickly at high energy than at low energy, as expected from energy losses. This is consistent with the result obtained in Delahaye et al. (2009) for secondary positrons. Nevertheless, above $\sim$10 GeV, we can observe that relativistic effects come into play and a difference appears between the Thomson approximation case and the relativistic case. Indeed, the latter induces a longer propagation scale at high energy, and consequently softens the rise of the cumulative fraction. This would be slenderly

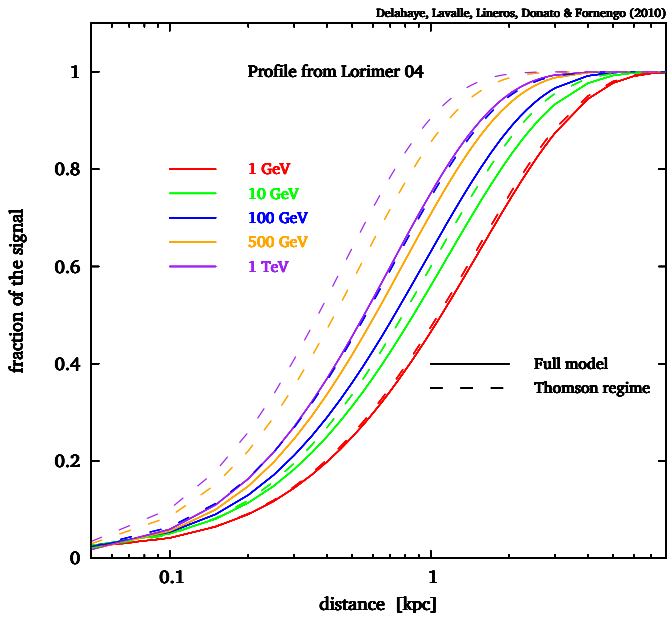

Fig. 6. Fraction of the signal reaching the Earth as a function of the integrated radius, for different energies and different spatial distribution models, using full relativistic energy losses. The Thomson approximation result is reported in dashed line.

less significant with a magnetic field of 3 μG instead of 1 μG, though still observable.

Another important information that we can get from Fig. 6 is that the cumulative signal fraction is $\gtrsim 95\%$ (80%) for $r \gtrsim 2$ kpc and $E \gtrsim 100$ (10) GeV. This will help to define consistent means to include local sources in our predictions, as we will discuss later in Sect. 4.4.2. Indeed, we know at present that if we replace the smooth spatial distribution within 2 kpc with discrete sources, the latter will affect the whole available energy range quite significantly: if powerful enough, local sources will dominate above a few tens of GeV, otherwise, flux predictions will be significantly depleted compared with a smooth-only description of sources, for a given normalization pattern.

4.3. Sizing the uncertainties for local sources

Before discussing the contribution of local known SNRs to the CR electron flux (see Sect. 4.4.2), it is essential to review the impact of uncertainties in the main parameters that describe the source. They are only a few, but their mixed effects on the flux will be shown to be important.

Aside from the propagation modeling and related parameters that were presented in Sect. 2.2 and Sect. 2.5, theoretical errors may originate from uncertainties (i) in the spectral shape and normalization, (ii) in the distance estimate and (iii) in the age estimate. The first point was discussed in Sect. 4.1, and is featured by two main parameters: the spectral index at source γ and the energy released in the form of high energy electron $f\,E_\star$, both related in the normalization procedure given Eq. (39) that allows to derive $\mathcal{Q}_\prime$. Points (ii) and (iii) have some impacts that can be understood from Sect. 2.2 and Sect. 2.3. Although the consequences of varying these parameters can be understood from equations only, we aim here to illustrate them in a more pedagogical way. To do so, we will consider a template event-like source located in the Galactic plane ($z = 0$) at a distance d to the Earth and bursting a population of electrons a time (age) $t_\star$ ago:

$$\mathcal{Q}_\star(t_s, E_s, \boldsymbol{x}_s) = \delta(t_s - t_\star)\,\delta(z_s)\,\delta^2(r_s - d)\,\mathcal{Q}(E_s)\ , \qquad (51)$$

where the spectrum $\mathcal{Q}(E_s)$ is given by Eq. (38). We will assume here that $f\,E_\star = 2 \times 10^{47}$erg.

In Fig. 7, we plot the electron flux for different configurations of the parameters, the default configuration being defined by: *med*, $\gamma = 2$, $E_c = 10$ TeV.

In the top left panel (a), we show the source age effect; in the top right panel (b), we illustrate the distance effect; in the bottom left panel (c), we sketched the spectral index effect; while in the bottom right panel (d), we plot the propagation model effect. For all panels, we report the fluxes calculated in both the Thomson approximation and the full relativistic treatment of the energy losses, as discussed in Sect. 2.4 and Sect. 2.5.

As a first comment, we emphasize that the Thomson approximation can lead to a very strong under-estimate of the spectral break inferred from energy losses, up to one order of magnitude in the examples shown. This is a mere consequence of the over-estimate of the energy loss rate at high energy. The net effect obviously depends on the magnetic field and on the actual cut-off considered at the source. As regards the latter, we see that using a value of 10 TeV already induces an under-estimate by a factor of ∼5-10 of the break predicted in the non-relativistic regime. Note that many of recent studies on the topic have employed the Thomson approximation.

The second important comment to make is that it is actually quite difficult to relate the observed spectral index to the source spectral index, because of the complex and degenerate effects coming from all parameters: distance, age, source index, energy cut-off, normalization and diffusion coefficient. For instance, we see that a large diffusion coefficient (*min* model) can make a source of 300 kyr (c) look like a source of 30 kyr (a) associated with a larger diffusion coefficient and a lower energy cut-off. In any case, a mere overlook at the four panels Fig. 7 is striking enough.

This exhaustive analysis of the impact of the main parameters characterizing individual sources already points towards the difficulties that we will encounter in the interpretation of the data. Nonetheless, although this part might look depressing at first sight in the perspective of making predictions, it will still be very useful to size the theoretical confidence level of our forthcoming attempts.

4.4. Primary electron flux and theoretical uncertainties

In the previous parts of this section, we have discussed the main physical quantities relevant for predictions of the primary electron flux at the Earth, emphasizing their role as potential sources of uncertainties. Here, we implement the full calculation and compare our results with available data on the electron flux. We stress that pure electron data are not numerous and rather old, since most of recent experiments either do not distinguish electrons from positrons or did not release their separate data yet. In this part, we will therefore only use the electron data from CAPRICE (Boezio et al. 2000), HEAT (DuVernois et al. 2001) and from AMS-01 (Alcaraz et al. 2000), in order to

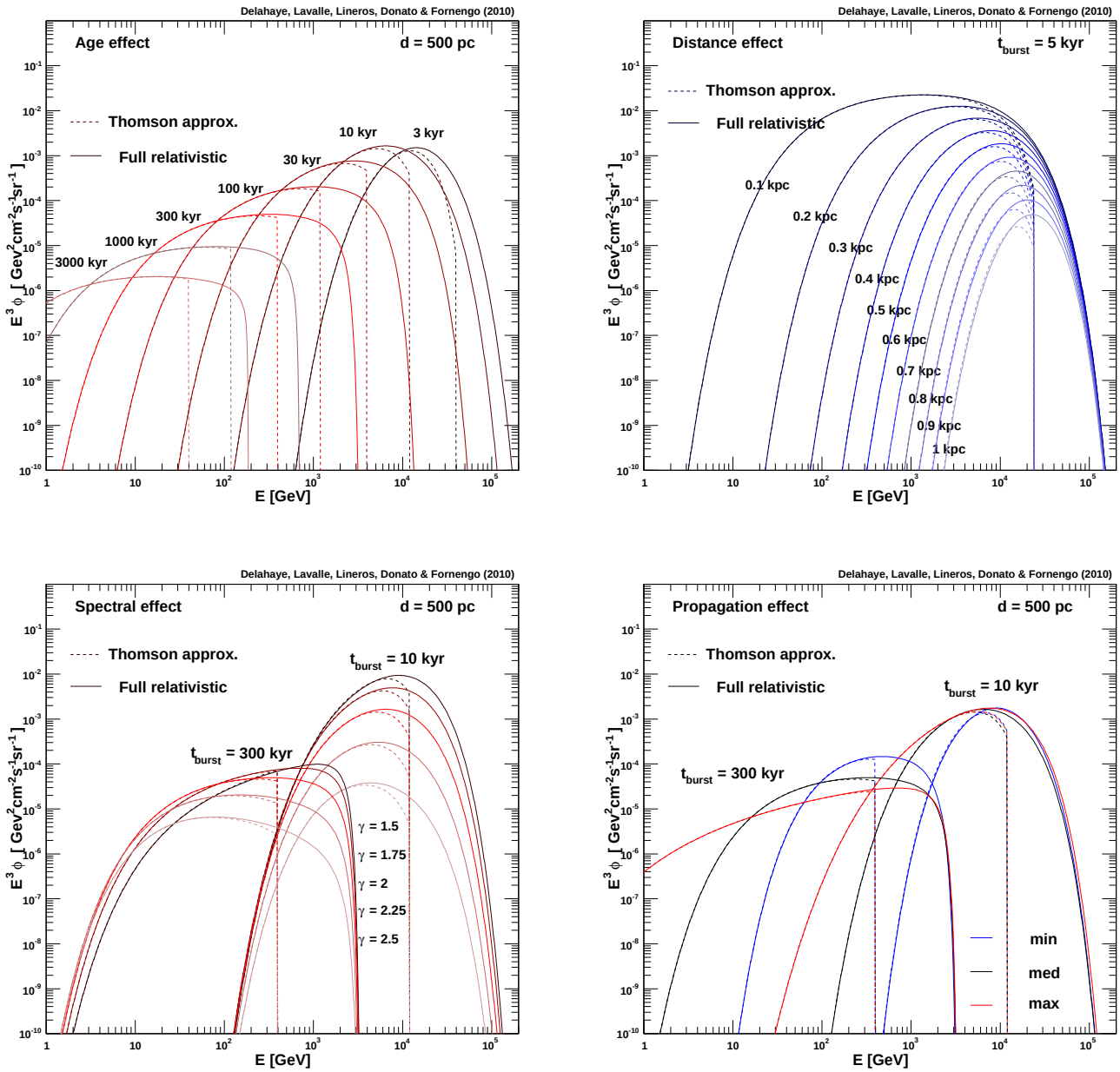

Fig. 7. Main uncertainties associated with the flux of primary electrons injected from a single bursting source. Top left: varying the age at a fixed distance of 500 pc — notice that taking 1 kpc would have suppressed the 3 kyr source for causality reasons. Top right: varying the distance for a fixed age of 5 kyr. Bottom left: varying the spectral index for fixed age of 5 kyr and fixed distance of 500 pc. Bottom right: varying propagation parameters, with the *min*, *med* and *max* setups from Tab. 1.

avoid any confused interpretation mixing positrons. The pure positron case and the full case will be discussed in Sect. 5 and Sect. 6 respectively.

We will first compare the predictions arising from a smooth description of sources, for which we will adopt the L04 spatial distribution. Indeed, we have shown in Sect. 4.2 that using different spatial distributions only results into small differences in the overall flux normalization locally.

Then, we will estimate the contributions of all known local SNRs that can be added to a smooth and more distant component, following the method proposed in Kobayashi et al. (2004).

4.4.1. Smooth description of sources

Our model for a smooth distribution of SNRs includes a propagation setup, a spatial distribution (here L04) and an injected spectrum, and it is interesting to check some of the possible configurations against the data. In particular, we will try constrain the injection normalization necessary for a model to fit, at least roughly, the data. For the spectrum, we will test different spectral indices, but will keep the energy cut-off at 3 TeV. As a reference normalization, we will use a SN explosion rate of 4/century, a SNR total energy of $E_\star = 10^{51}$ erg, of which a fraction of $f = 2\times10^{-4}$ is carried by electrons, giving therefore $\widetilde{\Gamma}_E = 8 \times 10^{47}$ erg/century.

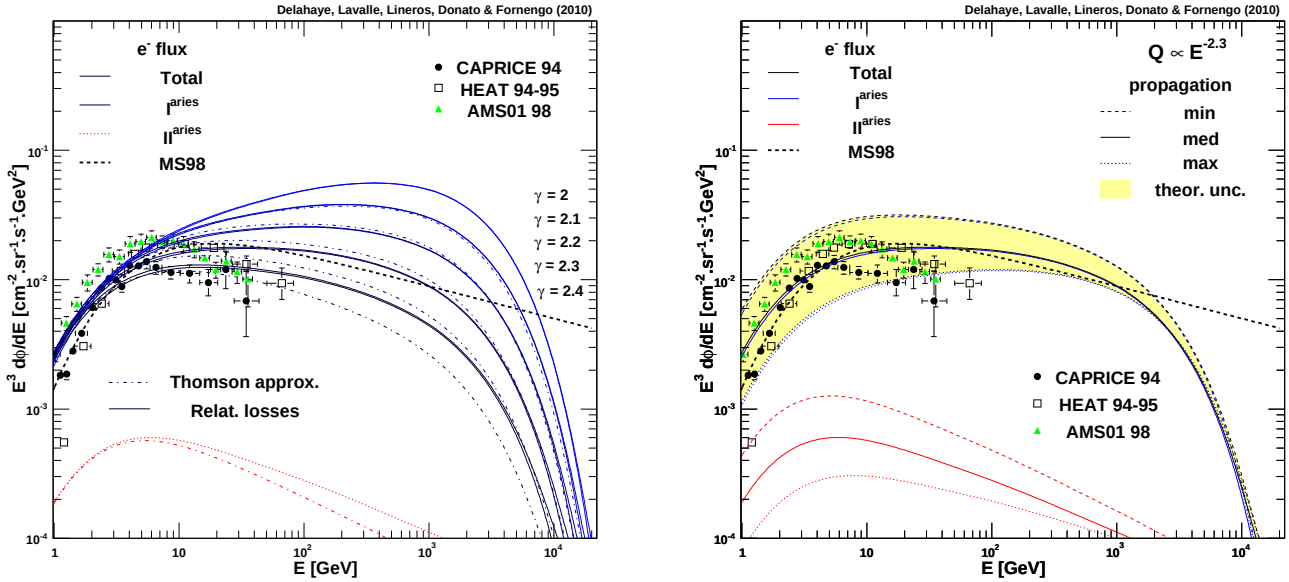

Fig. 8. primary electron flux from a smooth distribution of SNRs. Left: fluxes associated with injection indices γ from 2.0 to 2.4. Right: propagation effect for $\gamma = 2.3$. A renormalization factor of 5 has been applied to $\widetilde{\Gamma}_E$ in both panels and a cut-off energy of 3 TeV has been considered.

In Fig. 8, we report various flux calculations, for which we have further applied a solar modulation correction with a Fisk potential of 600 MV. In the left panel, we show the effect of varying the injected spectral index from 2 to 2.4 for the *med* propagation setup, using both the Thomson approximation and the relativistic regime for the energy losses. In this plot, we have renormalized $\widetilde{\Gamma}_E$ by a factor of 5 for all indices, so that we see that reasonable fits to the data can be obtained within the expected normalization range discussed in Sect. 4.1. This means that the expected energy budget available for electrons is in rough agreement with what is needed to explain the current observations. From the same plot, we could also conclude that the injection spectral index should be slightly softer than 2. Nevertheless, this also depends on the logarithmic slope δ of the diffusion coefficient, as seen from Eq. (21) — note that complementary constraints on $\gamma + \delta$ could also be derived from high energy proton data, under the assumption that the proton index is the same as the electron index after their acceleration at sources and that proton propagation is simply described by diffusion (*i.e.* no reacceleration nor convection). This is illustrated in the left panel of Fig. 8, where we show the effect of the theoretical uncertainties on the propagation parameters, using the same spectrum normalization and the same spectral index for all models. We see that the *min* model gives the larger amplitude because of its smaller value of K_0 and the softer observed index due to its larger diffusion slope δ (see Tab. 1 and Eq. 20) — the analysis is reversed in the *max* configuration. For a given normalization, the amplitude uncertainty is therefore proportional to $\sqrt{K_0}$, which gives a factor of ~ 7 from the *min* to the *max* configurations. In both panels of Fig. 8, we have also reported the prediction obtained in Moskalenko & Strong (1998), as fitted in Baltz & Edsjö (1998), where the authors used an injection index of 2.1 below 10 GeV, steepening to 2.4 above. This model, very often quoted a reference model, does not include relativistic losses, but is shown for comparison.

It should be noted that since the data have a quite limited statistics and range up to $\sim$ 40 GeV only, they are likely insufficient to provide strong constraints on the electron cosmic ray component. Moreover, such a smooth description of the SNR contribution is probably not valid locally above a few tens of GeV, where we expect discrete effects to become important. Nevertheless, such a preliminary analysis is still useful to delineate the relevant ranges for the spectral index and for the injected energy. Likewise, it will help to better size the influence of distant sources with respect to local ones.

Finally, we stress that we only considered here a single contribution from a SNR population. Nevertheless, we remind that electron-positron pair injection from pulsars is also likely to account for a significant additional contribution to the local electron budget. It is not clear whether this contribution should have the same spectral index, and one could for instance model the smooth electron component with a combination of two spectral components, leading to an additional freedom in the normalization procedure. This electron component from pulsars will be discussed in Sect. 5.

4.4.2. Contributions from known local sources

As discussed earlier, contributions from local sources are expected to be significant above a few tens of GeV. Following the method proposed in Kobayashi et al. (2004), we wish to take a census of all known sources of primary electrons located within 2 kpc from the Earth in order to compute their associated flux explicitly.

To proceed so, we first took advantage of the information provided in the SNR catalog of Green (2009), beside which we made an extensive synthesis of all pub-

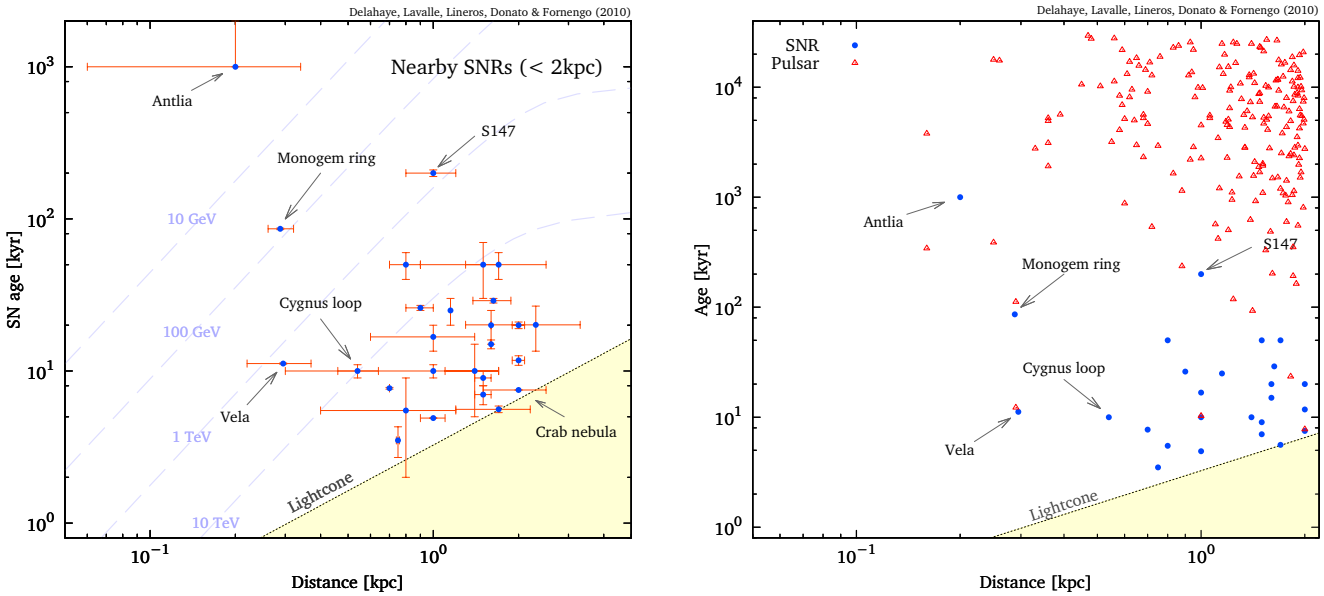

Fig. 9. Left: Plot of the *observed* age versus distance to the Earth for our sample of local SNRs (and associated uncertainties, see Tab. C.1). The dashed lines correspond to limits beneath which a local source cannot contribute significantly to the signal at the corresponding energy (valid only in the *med* propagation model — see Tab. 1). Indeed the age sets an upper limit, while the distance sets a lower limit to the energy range – see Sect. 4.4. Right: Same plot for our complete sample of local SNRs and pulsars.

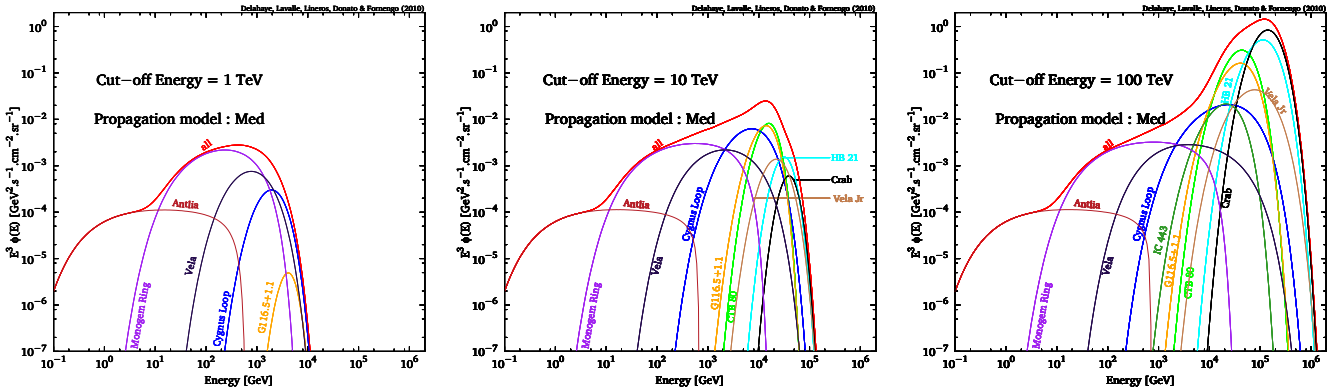

Fig. 10. Primary electron flux from local SNRs in the *med* propagation model and using radio observation constraints. Left: energy cut-off at $E_c = 1$ TeV. Middle: $E_c = 10$ TeV. Right: $E_c = 100$ TeV.

lished properties and associated errors (mostly from radio data). We have found 26 SNRs within 2 kpc in this catalog, to which we have added an extra-object, Antlia SNR (McCullough et al. 2002; Shinn et al. 2007). A full description of these sources including information on distance, age, spectral index, radio flux, associated objects and bibliographic references is available in App. C. These properties are summarized in Tab. C.1.

The event-like contribution of a single source is readily computed from the results obtained in Sect. 2.2. As a word of caution, however, we stress that the time argument used to feed the time-dependent propagator given in Eq. (18) should not be the *observed* age of the object given in catalogs, but instead the *actual* age, equal, in principle, to the observed age plus d/c. Indeed, most of the age estimates rely on the dynamical properties of the objects inferred from multi-wavelength observations, which correspond to the properties the object had a time d/c ago. As regards the injection spectrum, we use Eq. (38) and set the spectral index γ from the observed radio index γ_r — $\gamma = 2\gamma_r + 1$. We further constrain the spectrum normalization with the observed radio flux by means of Eq. (46).

Although SNRs are expected to provide an important contribution to the primary electron flux, we emphasize that pulsars are also expected to produce and accelerate electron-positron pairs. Modeling the electron injection from pulsar will be discussed in more details in Sect. 5, to which we refer the reader. Anyway, we found that ~ 200 pulsars located within a distance of 2 kpc from the Earth can actually feed the electron budget, among which few dominate (see Sect. 5.2). For consistency reasons, we have to include the contribution of these pulsars to the electron flux.

An additional important remark concerns the non-observed local sources of primary electrons that *should* exist. So far, we have listed 27 SNRs and about 200 pulsars. Nevertheless, it is worth recalling, as it will be delved into more details in Sect. 5, that pulsars are rotating neutron stars originating from core collapse supernova explosions. Therefore, each pulsar should be accompanied by a SNR.

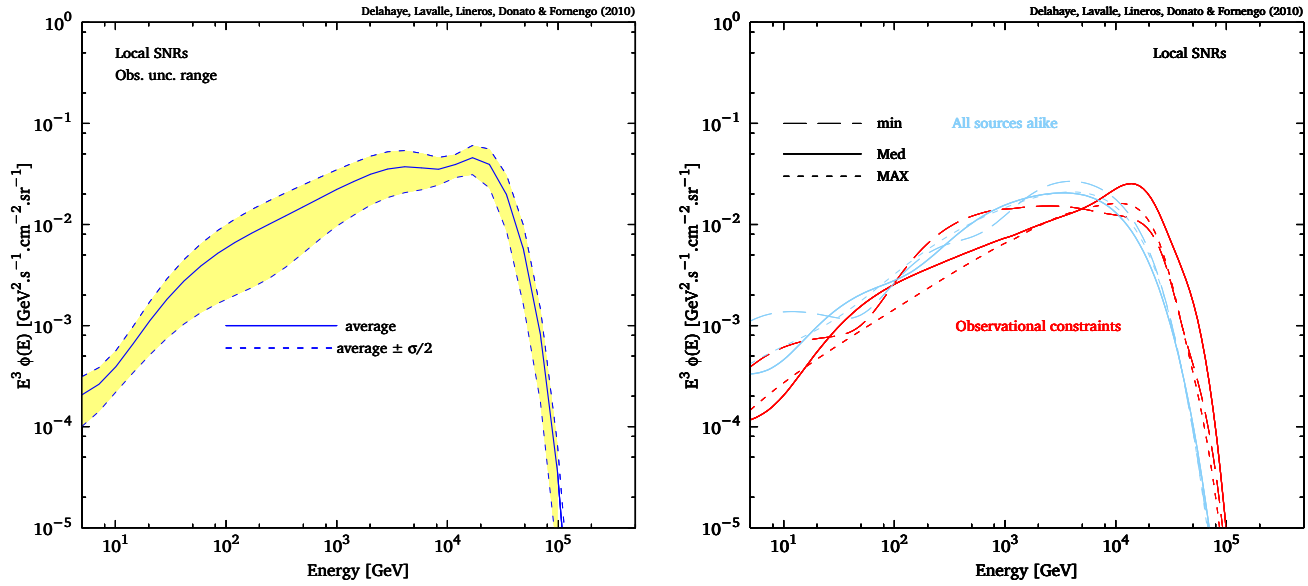

Fig. 11. Left: Electron flux from observed local SNRs, with associated uncertainty band (due to observational uncertainties on ages, distances, radio fluxes and spectral indices). Right: Propagation effects on the electron flux originating from local SNRs, using either the observational constraints or the average flux and index from Fig. 4. In both panels, we have assumed a source cut-off energy of 10 TeV.

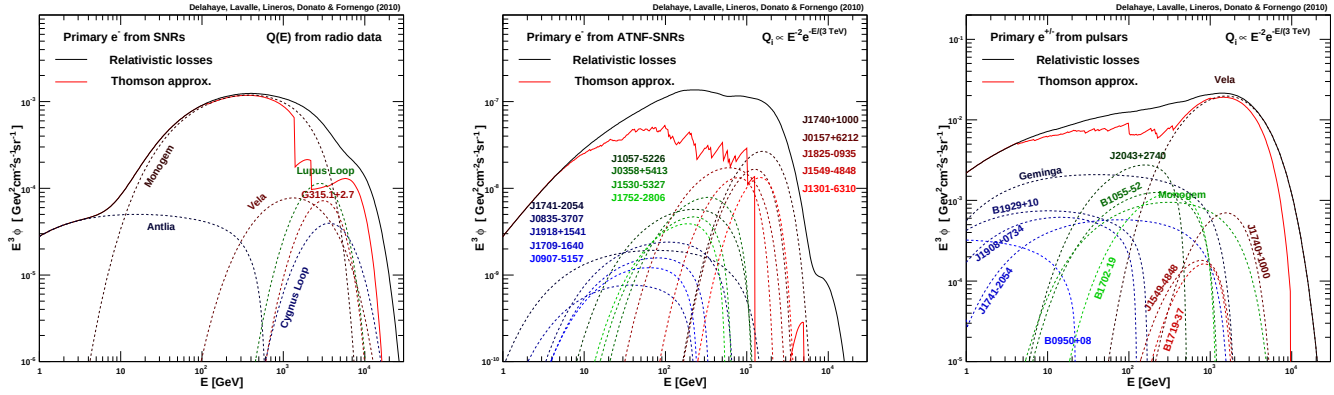

Fig. 12. Primary electron flux from local sources located within 2 kpc from the Earth. Left: from know SNRs (radio constraints). Middle: from unknown SNRs that should accompany unassociated local pulsars (generic spectrum for each, age and distance from the pulsar companion). Right: from known pulsars (generic spectrum, observational constraints on age and distance). Here, all generic spectra refer to a spectral index of 2 and an energy cut-off of 3 TeV.

Such a systematic association is obviously not supported by observations. This is already illustrated in our object list, in which we find only 27 SNRs for 200 pulsars. Moreover, among these 27 local SNRs, only 10 have a known pulsar counterpart (very often with differences in the distance and age estimates). Yet, this certainly does not mean that the theoretical expectation is wrong, but instead that the counterparts are probably not brighter enough to be observed. Therefore, again for theoretical consistency reasons, we choose here to add a SNR counterpart to each non-associated pulsar, but with a brightness such that it could not be observed with current telescopes. We have adopted $B(1\,\mathrm{GHz}) \lesssim 1\,\mathrm{Jy}$ as a general criterion for non-observed SNRs. Note finally that this local statistics can be tested against predictions of the SN explosion rate $\Gamma_\star$. If we assume at zeroth order that sources are distributed homogeneously inside a flat disk of radius $R = 20$ kpc, then the local explosion rate within a radius of $r = 2$ kpc around the observer merely reads $\Gamma_\star(r/R)^2 = 0.01 \times \Gamma_\star$, leading to $\sim$0.01 SN/century for usual values of $\Gamma_\star$. This can be compared to the observed local explosion rate, which we can estimate from the number of sources in our sample divided by the oldest age, *i.e.* $\sim 200/30\,\mathrm{Myr} \simeq 0.7 \times 10^{-3}$/century. This rough calculation leads to a difference of only a few, which would tend to tell us that using only the observed sources translates into a slight under-estimate of the actual local electron budget. This makes sense, since observations favor the brightest objects. Our samples of local SNRs and pulsars are shown in the age-distance plane in Fig. 9.

In Fig. 10, we show the electron flux obtained in the *med* propagation setup, using the local SNR properties summarized in Tab. C.1 and assuming different cut-off en-

	E_c	1 TeV	10 TeV	100 TeV
min	$\gamma = 2.0$	5, 20, 22, 24	+ 23	+ 8, 18, 19, 26
	$\gamma = 2.2$	5, 20, 22, 24	+ 8, 18	+ 17,19
	$\gamma = 2.4$	5, 20, 22, 24	+ 8, 17, 18	+ 19
med	$\gamma = 2.0$	5, 20, 22, 24, 26	+ 4, 11, 19	+8, 18, 23
	$\gamma = 2.2$	5, 11, 20, 22, 24	+ 4, 8, 18,23	+ 19
	$\gamma = 2.4$	5, 11, 20, 22, 24	+ 4, 18, 19, 23	+ 8, 17
max	$\gamma = 2.0$	5, 20, 22, 24, 26	+ 8, 11, 19, 23	+ 4, 18
	$\gamma = 2.2$	5, 20, 22, 24	+ 8, 11, 18, 19	+ 4, 23, 26
	$\gamma = 2.4$	5, 20, 22, 24	+ 8, 11, 18, 19	+ 4, 23, 24

Table 3. Ranked *id* numbers (see Tab. C.1) of those SNRs which contribute more than 10% of the signal for various propagation models, cut-off energies ϵ_c and spectral index γ. Index γ is only used for sources that are not constrained by radio data. The dominant sources are Cygnus Loop (5), Monogem Ring (20), Vela (22) and Antlia (24).

ergies. The first important comment to make is that the whole flux is far from being described from a mere smoothly injected power law, since many spectral wave-like features show up. Moreover, because of the interplay between the age and the maximal energy (see Sect. 2.2), we see that varying the energy cut-off from 1 to 100 TeV, though the latter value is probably not realistic and too high, leads to considerable effects. Not only do new contributions arise at high energy when the cut-off value increases, but also the hierarchy among other sources is altered. This illustrates an additional source of theoretical uncertainty, beside those we discussed in Sect. 4.3. Fig. 11 further illustrates the theoretical and observational uncertainties affecting both the source modeling and the propagation modeling. The left panel allows to bracket the impact of the observational uncertainties on the ages, distances, radio fluxes and spectral indices. This plot was made from 1,000 Monte Carlo realizations in which we drew each parameter according to a flat distribution within the observational errors. The right panel exhibits (i) the impact of varying the propagation parameters on the overall local SNR contribution and (ii) the difference arising from different injection spectrum prescription. For the latter point, we actually compared the flux obtained with generic spectral properties, namely a spectral index of 2 and a fixed normalization of $\mathcal{Q}_0 = 3.9 \times 10^{49} \mathrm{GeV}^{-1}$ (see end of Sect. 4.1), with the observationally constrained predictions. Again, we see that the global spectral shape is much more complex than a mere power law, and that the overall flux can vary within a factor of 2-5 depending on the energy.

We plot the results obtained with a template calculation for all local electron primaries in Fig. 12, where we have used the *med* propagation setup together with the M1 ISRF model (the large difference between the full relativistic calculation and the Thomson approximation is made explicit in the plots). The three panels from left to right show the contributions of local known SNRs, from non-observed SNRs associated with observed pulsars, and from observed pulsars, respectively. For the non-observed SNRs, we have taken the distances and ages of the associated pulsars, and we have assumed an injection spectrum with an index of 2 and a non-observable radio flux of $B(1\,\mathrm{GHz}) = 1\,\mathrm{Jy}$. While the contribution from the non-observed SNRs is shown negligible with respect to the two others, it is interesting to note that our local pulsar modeling leads to a larger primary electron flux than local SNRs. For pulsars, we actually assumed than 10% of the spin-down energy was converted into electron-positron pairs to set the individual normalizations (see Sect. 5). Although the injection mechanism is subject to large theoretical uncertainties, it is still rather surprising to find that even when accounting for observational constraints for pulsars, their local population can contribute as many primary electrons as the local known SNRs. We stress, however, that these calculations are subject to very large theoretical uncertainties, so no strong conclusions should be drawn: by no means should they be considered as predictions, only indications. The main conclusion at this stage is that nearby sources dominate the flux above few tens of GeV, the spectral imprints of which are very difficult to predict, due to large theoretical uncertainties in their modeling. Finally, it is clear from the plots that the Thomson approximation can lead to large errors in the predictions.

4.4.3. Electron flux: sum of distant plus local sources

We can now derive a full calculation including all known local sources within a distance of 2 kpc from the Earth and a more distant smooth component. For the latter, we will use the L04 spatial distribution, but at variance with what we did in Sect. 4.4.1, we further have to apply a radial cut-off to this smooth contribution within 2 kpc to the Earth, to avoid a possible double counting of the local sources. This means that the distant component will have more impact at low energy than at high energy.

Furthermore, we can also make comparisons with the available observational data on electrons. The top left panel of Fig. 14 shows an example of a calculation including all the components discussed above in a self-consistent manner, using the *med* propagation setup. To proceed, we have taken fixed all the parameter set from available observational constraints, and we have tuned the other parameters to provide a rough agreement of the calculated flux with the data. In particular, we have adjusted the global normalization and spectral index of the two distant smooth components (one for SNRs, another for pulsars) and of the local pulsars. The parameters that we used are summarized in Tab. 5.

5. Primary positrons

The rise observed in the positron fraction from the PAMELA data can hardly be interpreted in terms of secondary positrons (*e.g.* Delahaye et al. 2009), except with secondaries produced and accelerated in sources (Blasi 2009; Mertsch & Sarkar 2009; Ahlers et al. 2009). Some other more specific spatial arguments might also be relevant to deal with this issue (Shaviv et al. 2009).

Although exotic primary contributions from dark matter annihilation could contribute to the positron budget, the most popular dark matter particle candidates can hardly exceed the secondary background unless the annihilation

rate is substantially boosted (*e.g.* Baltz & Edsjö 1998; Lavalle et al. 2008a; Delahaye et al. 2008; Bergström et al. 2008), or the expansion rate is faster than expected in the early universe, before the primordial nucleosynthesis (see Salati 2003 for the original idea, and *e.g.* Catena et al. 2009 more specifically on the positron channel). Furthermore, the potential enhancement coming from dark matter substructures was demonstrated to be too small (see Lavalle et al. 2008b,a; Pieri et al. 2009), and any other type of global enhancement was shown to be severely constrained by the companion upper limit on the antiproton yield (*e.g.* Donato et al. 2009), which fully applies to the most popular dark matter models that have in no case exclusive couplings to leptons. We therefore emphasize that generic dark matter candidates are not expected, unfortunately, to manifest themselves in the positron spectrum in the GeV-TeV energy range.

As regards other potential sources of primary positrons, it is actually noteworthy that since the seminal work on electron-positron pair production in strong magnetic fields by Erber (1966), a particular class of cosmic ray sources has long been predicted to provide electron-positron pairs: pulsars (Sturrock 1970, 1971). It is not less noteworthy that a detailed discussion on the rising measured positron fraction and on the potential role of pulsars was already led two decades ago by Boulares (1989)[4]. Further deeper studies have been performed since then (*e.g.* Aharonian et al. 1995; Atoyan et al. 1995; Chi et al. 1996), which were recently revisited by several authors (*e.g.* Hooper et al. 2009; Profumo 2008; Yüksel et al. 2009; Malyshev et al. 2009). Since pulsars are commonly observed in the vicinity of the Earth, it is very likely that those standard and *existing* sources of positrons are at the origin of most of the local cosmic ray positrons. Nevertheless, many uncertainties remain in the characterization of pulsars, and there has been only little theoretical progress in the last decade.

We stress that making of pulsars a quite independent class of sources aside from SNRs is probably not justified, since they both originate from core collapse supernovæ: each pulsar should be, in principle, associated with a SNR. This is supported by observational facts since pulsar wind nebulae (PWNe) are sometimes found inside the shells of SNRs (see *e.g.* Gaensler & Slane 2006; Bucciantini 2008, for recent reviews on PWNe). Therefore, a more general picture of source modeling, at least for cosmic ray electrons and positrons, should involve a SNR as the main energy supply, and a pulsar and its PWN as a subsystem injecting additional high energy electrons and positrons (see *e.g.* Blondin et al. 2001).

In this section, we complement our calculations of the electron and positron flux at the Earth by including the contribution of pulsars. We will adopt the same methodology as for SNRs, and will consider two populations, (i) the local one, for which we will constrain the individual properties from observational data, and (ii) a more distant and smoothly described population. Like in most recent studies, the individual properties of pulsars will be derived from the ATNF catalog Manchester et al. (2005). In Sect. 5.1, we will sketch the generic model that we have adopted. In Sect. 5.2, we will discuss the contributions of both populations to the local electron and positron flux. Note that we will compare some template calculations to the current measurements of the positron fraction only further, in Sect. 6.2.

[4] Boulares (1989) did also mention that dark matter was another, though exotic, possibility.

5.1. Generic pulsar modeling

Independently of the specific pulsar model, like for instance the polar gap (Ruderman & Sutherland 1975), the outer gap (Cheng et al. 1976, 1986) or the slot gap (Harding et al. 2008) models, what concerns cosmic ray electrons and positrons can be summarized as follows. Gamma rays can be generated in the pulsar magnetosphere from inverse Compton processes of electrons accelerated along the strong and rotating magnetic field off local synchrotron radiation, which can further produce electron-positron pairs by annihilating with photons from the local radiation fields. Those gamma rays can be observed as a pulsed emission, like those recently discovered with the Fermi satellite (Abdo et al. 2009a), which may therefore be used to constrain the pair production. These electron-positron pairs are further accelerated within the surrounding and expanding shocked medium, at least in the phase of PWN, located inside or offset a more extended SNR. Observations of young systems like the Crab nebula tell us that this acceleration can be very efficient and lead to huge Lorentz factors, up to $\sim 10^8 - 10^9$ (Atoyan & Aharonian 1996). What is important when trying to predict the electron-positron yield from a pulsar is not their energy distribution and density close to the magnetosphere, but instead the final features after acceleration has proceeded and when particles are released in the ISM. This was already noticed and detailed in Malyshev et al. (2009). It is therefore rather difficult to provide accurate predictions when disregarding the whole dynamics at stake there, and, in this part, we mostly aim to survey the roles of the main ingredients that characterize pulsars rather than making peremptory predictions. Indeed, we will show in the following that current uncertainties still make it difficult to derive but qualitative predictions.

Following the arguments developed in Malyshev et al. (2009), to which we refer the reader for further details, we define the source term associated to any single pulsar as

$$\mathcal{Q}_p(E, \boldsymbol{x}, t) = q_p(E, t_\star)\, \delta(t - (t_\star + \delta t_\star))\, \delta(\boldsymbol{x} - \boldsymbol{x}_\star)\ , \qquad (52)$$

where $t_\star$ and $\boldsymbol{x}_\star$ are the pulsar age and position, respectively, and $\delta t_\star$ allows for a certain delay in the release of cosmic ray electrons in the ISM after the supernova explosion. Generic pulsars should have ceased their PWN phases after ∼10-100 kyr (Gaensler & Slane 2006); for simplicity, however, since characterizing the PWN evolution is far beyond our purpose here, we will assume that $\delta t_\star = 0$ in the following. The pulsar age is usually estimated from the *spin-down age* (Ostriker & Gunn 1969), only relevant in the spin-down magnetic radiation approximation, which involves the rotation period P and its first time derivative $\dot{P}$:

$$t_{\rm pulsar} = -\frac{P}{2\,\dot{P}}\ . \qquad (53)$$

Like in the SNR case, it is worth stressing again that such an age estimate relies on current observations, so that the *actual* age used for cosmic ray calculations should have an additional d/c term, where d is the distance of the pulsar to

the observer. We emphasize, however, that using the spin-down age for the pulsar age estimate turns out, in many cases, to be erroneous (see *e.g.* Gaensler & Frail 2000). Still, for simplicity, we will adopt this method to deal with local pulsars in the following.

For the energy spectrum, we adopt the same general shape as used previously for SNRs (see Eq. 38), *i.e.* a power-law of index γ with an exponential cut-off at energy E_c:

$$q_p(E) = \mathcal{Q}_0 \left(\frac{E}{E_0}\right)^{-\gamma} \exp\left(-\frac{E}{E_c}\right) . \quad (54)$$

Note that contrarily to the SNR case for which the spectral index can be constrained from radio observation, the spectral index associated with high energy electrons from pulsar can hardly be constrained from radio observations of the pulsed emission. Indeed, this pulsed emission originates from regions close to the pulsar magnetosphere, where the acceleration processes are not yet achieved. An alternative is to use the spectral indices derived from PWN observations, when available. To simplify, the discussion, we will use $\gamma = 2$ in the following, unless other values are specified.

The normalization $\mathcal{Q}_0$ is intimately linked to the total rotational energy W_0 of the pulsar, a fraction f of which is released in the form of electron-positron pairs, such that

$$\int_{E_{\rm min}}^{\infty} dE\, E\, q_p(E) \;=\; f\, W_0 \; . \quad (55)$$

W_0 can be constrained from measurements assuming that the whole energy lost is carried by the magnetic dipole radiation, such that

$$W_0 = \dot{E}\, \tau_{\rm dec} \left(1 + \frac{t_\star}{\tau_{\rm dec}}\right)^{\upsilon} , \quad (56)$$

where $\dot{E}$ is the spin-down luminosity and $\tau_{\rm dec} \equiv E_0/\dot{E}_0$ is the typical pulsar decay time. Notice that the index υ featuring the age dependence is in principle related to the braking index k which defines the rotation deceleration $\dot{\Omega} \sim -\Omega^k$, where Ω is the angular velocity, through $\upsilon = (k+1)/(k-1)$. In the spin-down approximation, $k = 3$, and therefore $\upsilon = 2$. Nevertheless, it turns out that k can also be computed if the second time derivative of Ω is known, $k = -\Omega\ddot{\Omega}/\dot{\Omega}^2$. In that case, it is usually found slightly different than 3.

Again, this illustrates the large degree of theoretical uncertainties arising when trying to model pulsars, even in simple approaches. Still, we will use the spin-down approximation, and will therefore fix $\upsilon = 2$ in the following.

Since accounting for the details in the pulsar modeling is beyond the scope of this paper, we will adopt the source model defined by Eqs. (52-56), and assume a universal decay time of $\tau_{\rm dec} = 1$ kyr. Using this latter input together with the ATNF data for the rotation period and its derivative, Malyshev et al. (2009) found typical values of $W_0 \sim 10^{49}$ erg, *i.e.* one or two orders of magnitude below the characteristic supernova energy release, in agreement with the picture of a pulsar as a subdominant energy supply beside its companion SNR. In the following, we will further assume by default that a fraction $f = 0.1$ of this energy is converted into electron-positron pairs.

For the nearby known pulsars, we will take the distances and the ages from the ATNF catalog. For more distant objects, say above a few kpc, we can safely use the continuous limit as we did for SNRs, and write the corresponding source term as

$$\widetilde{\mathcal{Q}}_p(E, \boldsymbol{x}) = \widetilde{q}_p(E)\, f(\boldsymbol{x}) . \quad (57)$$

The energy spectrum will be taken the same as in Eq. (54), but the normalization $\widetilde{\mathcal{Q}}_0$ will be set from an explosion rate similar to the case of SNRs.

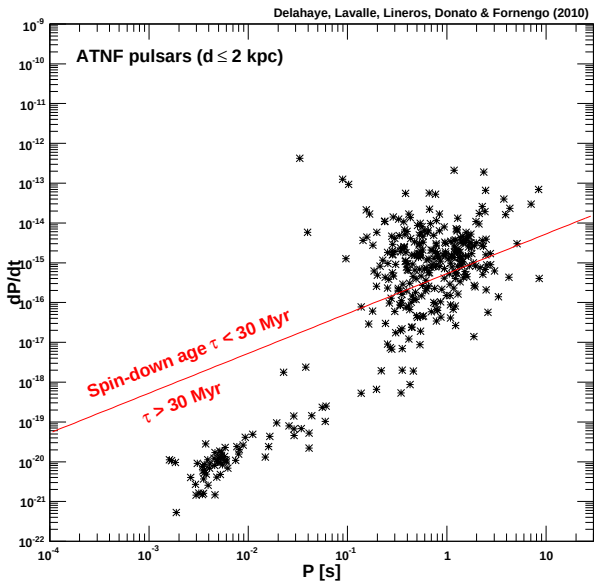

Fig. 13. Selection of local ATNF pulsars (within 2 kpc) in the $\dot{P} - P$ plane. Only

5.2. Local versus distant pulsars

We have selected local pulsars from the ATNF catalog, imposing few constraints. First, we have applied a radial cut-off of 2 kpc, like for the SNR treatment, farther pulsars being accounted for with a smooth spatial distribution modeling. For the latter, we have adopted the L04 model, as for distant SNRs (see Sect. 4.4.1 for more details). Moreover, considering energies above the GeV scale implies an upper limit of the pulsar age $\lesssim 30$ Myr, which shrinks down to 1 Myr above 100 GeV (see Fig. 7). Consequently, we will restrict our sample by requiring ages $\lesssim 30$ Myr. This selection procedure is depicted in Fig. 13, where the local ATNF pulsars are reported in the P-$\dot{P}$ plane. Our final sample contains a bit more than 200 objects located at less than 2 kpc from the Earth, which is quite large compared to the number observed SNRs, *i.e.* 27, discussed in Sect. 4.4.2.

The positron flux derived from this pulsar selection is actually the same as the pulsar contribution to the electron flux discussed in Sect. 4.4.2, because of the pair production mechanism. This local contribution is shown in the right panel of Fig. 12. We remind the reader that a SNR counterpart was systematically added to each local pulsar, except for those pulsars which have already an observed and identified SNR counterpart featuring in our SNR list. In case of non-observed SNR counterpart, we have assumed a

J2000	other name	distance [kpc]	spin-down age [kyr]	spin-down energy [10^{49} erg]	Rank @ 5/100/1000 GeV	known SNR counterpart
J0633+1746	Geminga	0.16	342	1.25	1/2/4	
J1932+1059	B1929+10	0.36	3,100	11.9	2/ø/ø	
J1908+0734		0.58	4,080	17.9	3/ø/ø	
J1741-2054		0.25	387	0.47	4/5/ø	
J0953+0755	B0950+08	0.26	17,500	54.2	5/ø/ø	
J2043+2740		1.13	1,200	25.9	ø/1/ø	
J1057-5226	B1055-52	0.72	535	2.8	ø/3/ø	
J0659+1414	B0656+14	0.29	111	0.18	ø/4/2	Monogem
J0835-4510	B0833-45	0.29	11.3	0.99	ø/ø/1	Vela
J1740+1000		1.24	114	1.1	ø/ø/3	
J0742-2822	B0740-28	1.89	157	1.23	ø/ø/5	
J1549-4848		1.54	324	0.8	ø/ø/6	

Table 4. Main positron sources among the ATNF nearby pulsars. We rank the pulsars from the largest contribution to the flux in different energy bins, assuming a spectral index of $\gamma = 2$ and a cut-off energy of 1 TeV. All other parameters are derived from the ATNF catalog.

radio flux $B(1\,\mathrm{GHz}) = 1\,\mathrm{Jy}$ to set its spectrum normalization (see Sect. 11). These non-observed SNR counterparts contribute to the electron flux only, which is reported in the middle panel of Fig. 12.

As shortly mentioned in Sect. 4.4.2, we emphasize that using the magnetic radiation approximation to constrain the energy released in the form of electron-positron pairs makes pulsars important sources of local high energy electrons and positrons, as intense as the observed local SNRs. We have used a pair conversion efficiency of $f = 0.1$ in this calculation, which might be optimistic, but still, decreasing this efficiency down to a few percent would still lead to a quite significant contribution to the local electron and positron budget. It is noteworthy that only the local positron flux is dominated by a few objects only among our ∼200 selected objects. The main sources and their properties are listed in Tab. 4. Although pulsar modeling is subject to many and large theoretical uncertainties, and despite the simplistic model we have employed to set the individual normalizations, our results suggest that SNRs might not be the only prominent sources of electron and positron cosmic rays. Nevertheless, such a complete approach involving pulsars and SNRs in a self-consistent framework remains to be studied in deeper details, which may be promising for further insights in the understanding of cosmic ray leptons.

A full template calculation of the positron flux including secondaries and primaries from distant and local pulsars is compared with existing data in the bottom left panel of Fig. 14. We have used the data from HEAT (DuVernois et al. 2001), CAPRICE (Boezio et al. 2000) and AMS-01 (Alcaraz et al. 2000), which provide constraints at energy less than ∼20 GeV only. From this plot, we see that secondaries can already account for a large fraction of the low energy positron flux, which is rather constraining for the additional primaries. In fact, we have some freedom to tune the normalization and the spectral indices of the distant and local component, since they are poorly constrained. For the normalization, we have to adjust the pair conversion efficiency f to values lower than 0.1, which reinforces the idea that pulsars can contribute to the local electron and positron flux quite naturally. This will be further discussed when touching upon the positron fraction in Sect. 6.2. Likewise, there is no particular need for using hard spectral indices $\lesssim 2$. The parameters that we have used are summarized in Tab. 5.

Finally, as for local contributions to the electron flux, we again point out that using the Thomson approximation to deal with the energy losses can lead to large errors and fake predictions of very peaky features in the overall positron spectrum.

6. Full electron and positron results — discussion

In this section, we aim at performing a template calculation with reasonable parameters for all previously discussed ingredients in order to demonstrate that standard astrophysical processes can rather easily account for current measurements. It is actually quite simple to find configurations in good agreement with the data of the sum of electrons plus positrons or/and on the positron fraction, but it is much more difficult to find additional agreement with the separate electron and positron data. We stress that many other studies have only focused on few of these data sets, more rarely on all together.

As an important and preliminary remark, we want to emphasize that playing with the parameters associated with very few local sources within reasonable ranges allows to fit all the data quite easily, by adjusting the low/high energy source hierarchy. Nevertheless, for the sake of illustration, we will try to use the full set of observational constraints that we dispose of without turning around. This will illustrate how difficult and complex such a self-consistent exercise can be. Yet, to simplify the discussion, we will stick to the *med* set of propagation parameters, keeping in mind that uncertainties affecting propagation lead to ~ 1 order of magnitude uncertainty in the overall predictions. For the solar modulation, we will use a Fisk potential of 600 MV.

Beside our template calculation, it is noteworthy that the data alone, assumed trustworthy, can already provide the *actual* separate positron and electron fluxes at the Earth. Indeed, let f_- and f_+ be the electron flux and the positron flux, respectively. Let us further assume that some fitting functions $f_{\rm tot}$ and $f_{\rm frac}$, for the measured total flux (*e.g.* from Fermi data) and for the positron fraction (*e.g.* from PAMELA data) respectively, exist and are known. Then we readily find:

$$f_+(E) = f_{\rm frac}(E) \times f_{\rm tot}(E) \quad (58)$$
$$f_-(E) = f_{\rm tot}(E)(1 - f_{\rm frac}(E)) \,. \quad (59)$$

Although we will not make the exercise in the following, we point out that obtaining individual predictions in good agreement with f_+ and f_- in the relevant energy range automatically ensures a good agreement with the measured positron fraction and total electron plus positron flux. This might sound tautological, but this is still a helpful method if one wishes to optimize her/his preferred CR model.

6.1. Electron and positron spectra: separate fluxes and sum

We aim at comparing a template calculation of the electron and positron fluxes to the available data. For electrons and positrons, as measured separately, we will use the data from CAPRICE (Boezio et al. 2000), from HEAT (DuVernois et al. 2001) and from AMS-01 (Alcaraz et al. 2000). Note that these data are quite poorly constraining at high energy, since they refer to energies below a very few tens of GeV, and are affected by large statistical errors for the largest available energy bins. Future data from PAMELA and AMS-02 will certainly provide much better separate constraints on these components. For the sum of electrons and positrons, we will employ the data from Fermi (Abdo et al. 2009b; Pesce-Rollins & for the Fermi-LAT Collaboration 2009), ATIC (Chang et al. 2008) and HESS (Aharonian et al. 2008, 2009a). Since we think it irrelevant to perform a fit, because of the large theoretical uncertainties, we will merely and empirically favor the data sets that have the smallest statistical errors whenever possible.

The top and bottom left panels of Fig. 14 show our template results for the electron flux and the positron flux at the Earth, respectively. The parameters that we have used to calculate all contributions are reported in Tab. 5.

For electrons, we see that the data of CAPRICE and AMS-01 are barely consistent, but we can manage to find a median configuration. Actually, our template model relies on a smooth SNR-plus-pulsar component (following the L04 spatial distribution) that fits the low energy part — the smooth pulsar contribution is actually completely negligible. Note that we have used a rather soft spectral index of 2.4 to arrange this low energy shape from the smooth contribution, and a rather large value of $\widetilde{\Gamma}_E$(still consistent with theoretical or observational constraints — see Sect. 4.1). Nevertheless, we point out that using another spatial distribution, for instance with a stronger/softer spatial gradient, could have given the same result with other appropriate spectral indices and normalizations (see right panel of Fig. 5). This smooth component quickly falls down beyond 10 GeV because of the 2 kpc radial cut-off that we have set around the Earth before adding the local component. Above 10 GeV, we see that the local SNR contribution comes into play, clearly dominating over local pulsars. We stress that this is not a prediction at all, since both types of sources are expected to provide similar amounts of electrons (see left and right panels of Fig. 12). Instead, we have adjusted the local SNR flux by a global factor of 6 with respect to our constraint recipe given in Eq. (46), which corresponds to using a mean magnetic field of $\sim 30\,\mu$G instead of 100. Actually, since few sources dominate the overall flux (see Fig. 12 and Tab. 3), modifying the associated intensity would give the same result. Notice that another pulsar to SNR contribution ratio could easily lead to a similar overall shape for the electron flux. Likewise, slightly relaxing our chosen constraints either directly on the individual intensities or on the ages and distances, even in quite limited ranges, would let much more freedom to shape each contribution differently. Yet, for the sake of the exercise, we have imposed a fixed source hierarchy for each local component (SNRs or pulsars) set from constraints based on observational data — see Eq. (46) for SNRs and Eq. (56) for pulsars; other methods based on different assumptions and different data would have obviously led to different results. Finally, it is interesting to note that the local source flux is not typified by individual prominent peaks, as it would result from the Thomson approximation for the energy losses (see Fig. 12). Further constraints on the sources of electrons come from the sum of electrons plus positrons and from the positron fraction, as we will discuss farther.

For the positron flux, the important comment is that secondaries are likely dominant below 5 GeV. Actually, the calculation of secondaries suffers less theoretical uncertainties, so that we could in fact consider this as a *prediction*. Indeed, since the progenitor proton flux is not expected to vary significantly within a few kpc, the main uncertainty beside propagation is the average gas density (Delahaye et al. 2009). Therefore, we could expect the low energy flux to vary at most by few tens of %, which somehow further justifies this statement. Beyond 5-10 GeV, there are poor constraints on the positron flux, so that the contribution of primaries could take any shape. The positron fraction will provide more information and constraints, as we will see a bit farther. Nevertheless, we see our choice of parameters for pulsars (distant and local) makes their contribution significant above ~ 5 GeV. From Tab. 5, it is noteworthy that assuming less than 1% of magnetic energy converted into electron-positron pairs is enough to make the pulsar contribution arise around 10 GeV; this is independent of the injected spectrum (we have taken a spectral index of 2). Not less noteworthy is that the smooth pulsar contribution turns out to be negligible with respect to the local one. Finally, we stress that the overall spectral shape obtained for the positron flux weakly depends, in fact, on the assumed spectral index for pulsars. Indeed, as already shown in the right panel of Fig. 12, we see that decreasing the intensity of few old sources (like Geminga or B1929+10) could easily result in a much harder spectrum at high energy while in an even lower contribution below 10 GeV. Therefore, better constraining the amplitude of the observed sources is a priority for future works.

The top right panel of Fig. 14 shows the sum of electrons plus positrons, consistently with the separate results that we have just discussed above. The cleaner information one can extract from this plot is probably the energy cut-off that explicitly appears around 1 TeV. This observational fact obviously imposes us to set a cut-off energy around that value. In our template calculation, the high energy part of the spectrum, above ~ 50 GeV, is actually dominated by our local SNR sample. We stress that this is not a prediction, since we could have arranged a dominating pulsar contribution by slightly modifying the injection parameters. For instance, we could have reduced the local SNR yield, depleted the supply from Geminga and increased that from Vela, and finally allowed a larger fraction of $\sim 2\%$ of pair conversion.

As a general comment at this stage of the game, we would like to emphasize that the current constraints on sources are actually by far too weak to claim for the predic-

	L04 SNRs	local SNRs (Green)	local SNRs (ATNF)	L04 pulsars	local pulsars (ATNF)
Spectral index	2.4	†	2.4	2.0	2.0
$\widetilde{\Gamma}_E$ [10^{48} erg/100 yr]	28	$6\times$ †	from $B(1\,\mathrm{GHz})=1\,\mathrm{Jy}$	2.0	†
Converted fraction [%]	ø	ø	ø	0.6	0.6
E_c [TeV]	2.0	2.0	2.0	1.5	1.5

Table 5. Injected energy, converted fraction, spectral indices and cut-off energies used for the overall template electron and positron flux calculation. The symbol † indicates that we sued observational constraints. For local SNRs, we have used a global extra-factor of 6, which corresponds to assuming a magnetic field of ~ 30 instead of 100 μG in Eq. (46).

tive power of our template calculation. Still it seems clear that the source modeling is the key point in the understanding of the high energy CR electrons, at least for identifying more clearly those few sources which may set most of the local flux. We also underline that it is important to challenge any CR electron prediction with the separate electron and positron data, since reproducing the sum does not necessarily ensure the relevance of the model. It will be important in the future to have much better separate data; PAMELA and AMS-02 carry many hopes.

6.2. Positron fraction

Measurements of the positron fraction offer additional constraints that should be fulfilled consistently with the previous data. In the bottom right panel of Fig. 14, we have used the data from HEAT (Barwick et al. 1997; Beatty et al. 2004), from AMS-01 (AMS-01 Collaboration et al. 2007) and from PAMELA (Adriani et al. 2010). From this plot, our template calculation turns out to be consistent with the data, especially above 10 GeV. Below, there are large discrepancies among the available measurements, which renders the interpretation complicated, though a more realistic treatment of the solar modulation — which is beyond the scope of this paper — might improve their level of consistency. What is important to note is that we are able to feature a slightly rising positron fraction with very reasonable parameters for the local pulsar modeling, without the need of tuning the sources individually. Indeed, for our local samples of SNRs and pulsars, we stress again that we have constrained the whole contributions from observational constraints and fixed assumptions. It would have been quite easy to make this fraction rising much faster with energy by considering other assumptions for the pulsar magnetic energy converted into electron-positron pairs. Here, we have considered the simplest approach of the spin-down approximation for which the injection rate dependency scales like the squared age (see Eq. 56). Should have we adopted another modeling with a shallower dependency in the age (see *e.g.* Chi et al. 1996; Zhang & Cheng 2001; Profumo 2008), we would have given more weight to younger objects, and thereby to the high energy part. As for the other measurements discussed above, we conclude that the positron fraction can be accommodated rather easily from standard astrophysics, even if the predictive power our calculation remains weak.

6.2.1. Final comments

As final comments, we may insist on few major points. First, it seems fair to state that standard astrophysics is enough to understand the existing data, despite the large theoretical uncertainties associated with the flux calculation. Second, we hope to have convinced the reader that an overall check of the separate electron and positron flux calculations against the associated separate data is mandatory to ensure the relevance of a model: this implies using the four sets of data used in Fig. 14 separately. Note that this is barely done in the recent literature, where most of the authors have mostly focused on the sum of CR electrons plus positrons or on the positron fraction. Third, we have shown that the full relativistic treatment of the energy losses could lead to a global spectral shape devoid of peaky structures. Fourth, we have discussed a template example where we have fixed the local source hierarchy from few assumptions and observational constraints. It is clear, however, that a more refined analysis with a much better source modeling will help to reduce the theoretical uncertainties and clarify the local source hierarchy; it will also probably lead to different results. Still, we have proposed an exhaustive set of analytical tools together with a robust method to tackle such a detailed analysis. Finally, we stress that we have derived our template calculation using our *med* set of propagation parameters to facilitate the reading of the plots, and have therefore not discussed the uncertainties coming from the propagation side. These are actually large, but were already discussed in Sect. 4.3 for individual sources (see bottom right panel of Fig. 7) — see also Fig. 11.

7. Conclusion

In this paper, we have tried to make an exhaustive study of the main ingredients relevant for the calculation of the high energy CR electron and positron fluxes in the GeV-TeV energy range. We have underlined the complexity arising in the source description, with emphasis on the potentially strong effects coming from nearby sources, and shown that though we can hardly predict the local electron and positron fluxes, reasonable parameterizations for the source and the propagation modeling can fairly well and simultaneously account for the current measurements on (i) electrons, (ii) positrons, (iii) the sum of them and (iv) the positron fraction. We summarize hereafter the way we have proceeded.

In Sect. 2, we have presented our propagation modeling in detail. We have reviewed the analytical solutions to the transport equation in Sect. 2.1 and Sect. 2.2 and de-

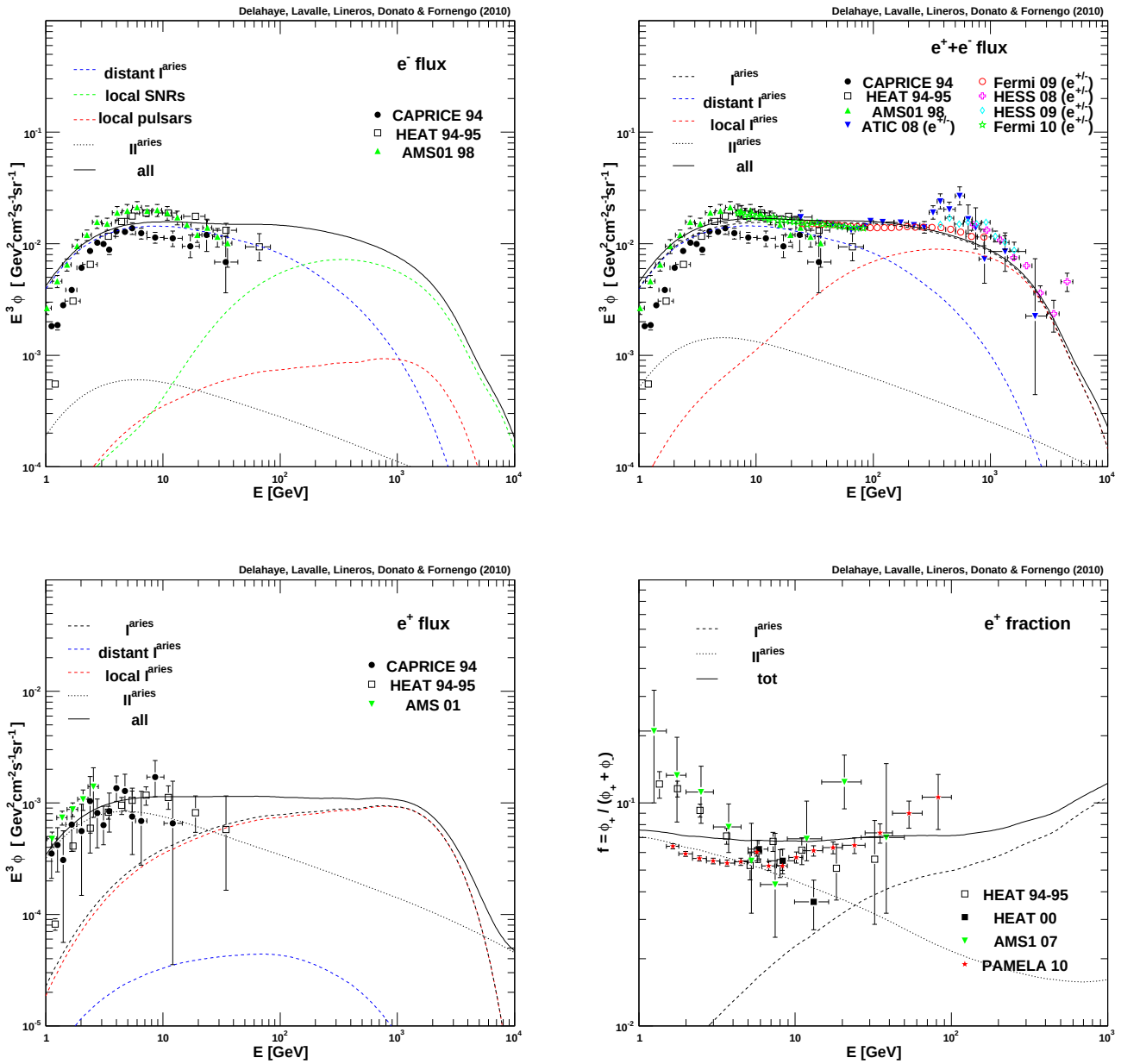

Fig. 14. Template calculation including all primary (discrete local and smooth distant) and secondary electrons and positrons in a self-consistent modeling, using the *med* propagation setup. Top left: electron flux. Top right: electron and positron flux. Bottom left: positron flux. Bottom right: positron fraction.

rived explicit links between the source spectrum and the propagated spectrum in Sect. 2.3. More important, we have developed in Sect. 2.4 a method to account for the relativistic energy losses, providing useful fit formulae that can be used for any inverse Compton processes involving a blackbody photon target. Indeed, we have further shown that the Thomson approximation was by far insufficient and could lead to fake predictions of peaky signatures in the electron spectrum as potential imprints of local sources. Then, in Sect. 2.5, we have recalled our propagation parameters with emphasis on the energy losses. In particular, we have worked out a rather constrained local ISRF modeling and explained in detail how its different components result in decreasing steps in the overall energy loss function, as a consequence of Klein-Nishina effects.

In Sect. 3, we have revisited the predictions for the secondary electron and positron fluxes, resulting in slight differences from the previous analysis we did in Delahaye et al. (2009) — on positrons only, and using the Thomson approximation for the energy losses. These differences are due to our novel relativistic treatment of the energy losses. Indeed, we now find a slightly harder secondary spectrum, with an overall flux larger by $\sim 10\%$ at 100 GeV up to $\sim 50\%$ at 1 TeV. We stress, however, that this can still not explain a rising positron fraction. We provide fitting formulae of our results in App. B, valid in the *med* propagation setup.

In Sect. 4, we have delved into the details of the calculation of the primary electron flux. We have thoroughly discussed the possible ways of normalizing the injection rate of CR electrons in Sect. 4.1, focusing on a smooth distribution of sources as well as on discrete sources, and shown that the theoretical uncertainties are impressively large, reaching 2 or 3 orders of magnitude. In particular, the fraction of energy transmitted to CR electrons is quite an issue. Still, we have sketched a method to normalize an event-like source injection density from its measured radio flux, which allows to use observational constraints whenever available. We have further demonstrated in Sect. 4.2 that any smooth spatial distribution of sources could be approximated with a mere z-exponential disk up to a very good accuracy for electrons above a few tens of GeV, showing that the specific spatial distribution had negligible impact on the predictions, for which only the local density of sources really accounts. Since local effects are dominant above a few tens of GeV, we have exhaustively studied in Sect. 4.3 the impacts of the parameters relevant for the local event-like source description, *i.e.* the age, the distance and the spectral index, as well as of the propagation parameters (see Fig. 7). We have notably illustrated how irrelevant the individual spectral indices were to infer the overall spectral shape originating from a population of non-identical objects. Instead, we have shown that the overall spectrum was mostly set by a hardly predictable hierarchy in the local sources. The energy range characterizing a single contribution is mostly bounded from above by the age and cut-off energy, and from below by the distance. As regards the former bound, we have demonstrated that the Thomson approximation led to erroneous predictions, with significant under-estimates of the maximal energy and fake peaky features. We have shown, however, that changing the diffusion coefficient had strong impact on the results. Finally, in Sect. 4.4, we have discussed a template calculation including the constrained contributions of all known local sources lying within a distance of 2 kpc from the Earth, showing that pulsars might contribute as many primary electrons as SNRs. We again emphasize the quite poor predictive power that can be achieved even when accounting for observational constraints. This is mostly due to the theoretical uncertainties affecting the source modeling. Still, we have provided a list of few objects which very likely dominate the overall high energy flux.

In Sect. 5, we have studied the contribution of pulsars to the primary positron flux, using the spin-down approximation to constrain the injection rate of local pulsars. As for primary electrons, we have shown that the very large theoretical uncertainties makes it difficult to claim for robust predictions.

Concerning the local sources, we have proposed a novel approach not only including known SNRs or pulsars, but also adding a SNR counterpart to each non-associated pulsar. Indeed, since a pulsar is the relic neutron star of a core collapse supernova explosion, it should be accompanied by a SNR for consistency reasons. We have obviously accounted for the fact that these non-observed SNRs must have a radio flux below the current experimental sensitivities when normalizing their injection rates of electrons. Note that conversely, all SNRs are not expected to have a pulsar companion, in particular those SNRs coming from SN1a explosions. Anyway, a more refined and realistic modeling of sources including such composite contributions and further accounting for the dynamics of CR injection remains to be translated in terms of electron flux. This is, however, far beyond the scope of this paper, though we hope to have paved the road for such an ambitious study.

Finally, in Sect. 6, we have presented a template calculation including all sources of primaries, in which we used observational constraints whenever available (see Fig. 14). We have thereby faced out the actual complexity of the source description within a self-consistent framework, at variance with many other studies merely adding local contributions on top of other so-called *standard* predictions. We have shown that with reasonable assumptions for the parameters of both the local and distant components, all of the discussed standard astrophysical processes can rather well account for all measurements of cosmic ray electrons and positrons independently. We have pointed out that comparing any prediction only with the positron fraction or the sum of electrons and positrons is incomplete, and does not ensure its consistency. Anyway, we emphasize that our template calculation is by no mean a prediction because of the very large theoretical uncertainties underlined along this paper. Instead, our results should be considered as a demonstration that current measurements are *compatible* with standard astrophysical processes, so that one can hardly claim for any prominent anomaly at the moment. More important, we hope to have shown that a *standard model* of CRs is far from being reached, since we even do not control the modeling of the local environment (mostly the sources) which is of paramount importance here. This may have drastic consequences; for instance, this gives indications on how well one really controls or predicts the CR electron contribution to the high energy part of the Galactic diffuse gamma-ray emission, or to the diffuse radio emission. Reversely, however, these diffuse emissions can provide additional information and constraints on the astrophysical processes at stake. Anyway, it seems that more *standardizable* predictions can only emerge for observables that involve features averaged over large spatial and/or time scales, to guaranty protection against potentially large and hardly controllable fluctuations in the calculation results. This is for instance the case for high energy stable nuclei.

Such conclusions might sound daunting but they actually suggest many interesting by-products, and open anyway a very broad landscape for future theoretical improvements. For instance, we have shown that few local sources may dominate the electron flux. If so, much more refined models for these sources can give hopes to use electrons as independent tracers of the local diffusion coefficient. Anisotropic diffusion might also be tested from electrons and could provide constraints on the power hierarchy among local sources, provided this hierarchy is strong; indeed, each flux energy-bin is likely filled by contributions from several sources located at different positions in the sky. In any case, the connection between the local CR electrons and the physics of sources is probably one of the most important issue to investigate further in future studies; low energy protons could also be used as additional constraints on the local sources.

Finally, as regards the searches for exotic signatures, coming for instance from dark matter annihilation or decay, the large theoretical uncertainties associated with the standard astrophysical processes prevent us to provide much stronger constraints, unfortunately. Nevertheless, we stress

that any exotic contribution is absolutely not necessary to understand the current data, and is therefore quite easily arguable. It seems therefore likely that models which are over-tuned to fit the positron data, aside from independent motivations coming from particle physics, are of very weak relevance. We remind the reader that almost all well studied dark matter particle candidates, *e.g.* in the frame of supersymmetric or extra-dimensional theories, are not expected to manifest themselves in the local positron nor antiproton spectra (*e.g.* Lavalle et al. 2008a; Delahaye et al. 2008; Donato et al. 2004). Should dark matter annihilation really feed the positron budget, much more work would be necessary to prove it, with a multi-messenger and a multi-wavelength approach. This still implies great efforts to face the complexity of the astrophysical backgrounds and, more important, this will have to rely on self-consistent calculations of both the signals and backgrounds.

Acknowledgements. We are deeply indebted to P. Salati for very inspiring comments and previous collaborations on related topics. We would like to thank A. Fiasson and Y. Gallant for very helpful discussions about SNRs and pulsars. We are also grateful to the participants of the two Workshops on Diffuse γ-ray emission, organized in 2008 and 2009 in the frame of the French GDR PCHE, for fruitful debates related to the topic[5]. TD thanks the International Doctorate on Astro-Particle Physics (IDAPP) and the Rhône-Alpes region (Explora'Doc program) for financial support. JL is grateful to LAPTH for hospitality during parts of this study. NF acknowledges support of the Spanish MICINNs Consolider–Ingenio 2010 Programme under grant MULTIDARK CSD2009-00064. This work was partly supported by research grants funded jointly by Ministero dell'Istruzione, dell'Università e della Ricerca (MIUR), by the University of Torino (UniTO), by the Istituto Nazionale di Fisica Nucleare (INFN) within the *Astroparticle Physics Project*, by the Italian Space Agency (ASI) under contract N° I/088/06/0 and by the French Programme National de Cosmologie (PNC).

References

Abdo, A. A., Ackermann, M., Ajello, M., et al. 2009a, Science, 325, 840
Abdo, A. A., Ackermann, M., Ajello, M., et al. 2009b, Physical Review Letters, 102, 181101
Abdo, A. A., Ackermann, M., Atwood, W. B., et al. 2008, Science, 322, 1218
Adriani, O., Barbarino, G. C., Bazilevskaya, G. A., et al. 2010, ArXiv e-prints
Adriani, O., Barbarino, G. C., Bazilevskaya, G. A., et al. 2009, Nature, 458, 607
Aharonian, F., Akhperjanian, A. G., Anton, G., et al. 2009a, A&A, 508, 561
Aharonian, F., Akhperjanian, A. G., Barres de Almeida, U., et al. 2008, Physical Review Letters, 101, 261104
Aharonian, F., Akhperjanian, A. G., de Almeida, U. B., et al. 2009b, ApJ, 692, 1500
Aharonian, F. A., Atoyan, A. M., & Voelk, H. J. 1995, A&A, 294, L41
Ahlers, M., Mertsch, P., & Sarkar, S. 2009, Phys. Rev. D, 80, 123017
Alcaraz, J., Alpat, B., Ambrosi, G., et al. 2000, Physics Letters B, 484, 10
Alvarez, H., Aparici, J., May, J., & Reich, P. 2001, A&A, 372, 636
AMS-01 Collaboration, Aguilar, M., Alcaraz, J., et al. 2007, Physics Letters B, 646, 145
Anderson, S. B., Cadwell, B. J., Jacoby, B. A., et al. 1996, ApJ, 468, L55+
Asano, M., Matsumoto, S., Okada, N., & Okada, Y. 2007, Phys. Rev. D, 75, 063506
Atoyan, A. M. & Aharonian, F. A. 1996, MNRAS, 278, 525
Atoyan, A. M., Aharonian, F. A., & Völk, H. J. 1995, Phys. Rev. D, 52, 3265
Baltz, E. A. & Edsjö, J. 1998, Phys. Rev. D, 59, 023511
Baltz, E. A. & Wai, L. 2004, Phys. Rev. D, 70, 023512
Barwick, S. W., Beatty, J. J., Bhattacharyya, A., et al. 1997, ApJ, 482, L191+
Battiston, R. 2007, Nuclear Physics B Proceedings Supplements, 166, 19
Beatty, J. J., Bhattacharyya, A., Bower, C., et al. 2004, Physical Review Letters, 93, 241102
Berezinskii, V. S., Bulanov, S. V., Dogiel, V. A., & Ptuskin, V. S. 1990, Astrophysics of cosmic rays (Amsterdam: North-Holland, 1990, edited by Ginzburg, V.L.)
Bergström, L., Bringmann, T., & Edsjö, J. 2008, Phys. Rev. D, 78, 103520
Blair, W. P., Sankrit, R., & Raymond, J. C. 2005, AJ, 129, 2268
Blair, W. P., Sankrit, R., Torres, S. I., Chayer, P., & Danforth, C. W. 2009, ApJ, 692, 335
Blandford, R. & Eichler, D. 1987, Phys. Rep., 154, 1
Blasi, P. 2009, Physical Review Letters, 103, 051104
Blasi, P. & Serpico, P. D. 2009, Physical Review Letters, 103, 081103
Blondin, J. M., Chevalier, R. A., & Frierson, D. M. 2001, ApJ, 563, 806
Blumenthal, G. R. & Gould, R. J. 1970, Reviews of Modern Physics, 42, 237
Boezio, M., Carlson, P., Francke, T., et al. 2000, ApJ, 532, 653
Bonatto, C. & Bica, E. 2009, MNRAS, 278
Borka Jovanović, V. & Urošević, D. 2009, ArXiv e-prints 0904.2261
Boulares, A. 1989, ApJ, 342, 807
Brisken, W. F., Thorsett, S. E., Golden, A., & Goss, W. M. 2003, ApJ, 593, L89
Brogan, C. L., Gelfand, J. D., Gaensler, B. M., Kassim, N. E., & Lazio, T. J. W. 2006, ApJ, 639, L25
Bucciantini, N. 2008, Advances in Space Research, 41, 491
Bulanov, S. V. & Dogel, V. A. 1974, Ap&SS, 29, 305
Burrows, A. 2000, Nature, 403, 727
Bykov, A. M., Krassilchtchikov, A. M., Uvarov, Y. A., et al. 2004, A&A, 427, L21
Byun, D.-Y., Koo, B.-C., Tatematsu, K., & Sunada, K. 2006, ApJ, 637, 283
Caraveo, P. A., De Luca, A., Mignani, R. P., & Bignami, G. F. 2001, ApJ, 561, 930
Case, G. L. & Bhattacharya, D. 1998, ApJ, 504, 761
Castelletti, G. & Dubner, G. 2005, A&A, 440, 171
Castelletti, G., Dubner, G., Golap, K., et al. 2003, AJ, 126, 2114
Catena, R., Fornengo, N., Pato, M., Pieri, L., & Masiero, A. 2009, ArXiv e-prints
Cha, A. N., Sembach, K. R., & Danks, A. C. 1999, ApJ, 515, L25
Chang, J., Adams, J. H., Ahn, H. S., et al. 2008, Nature, 456, 362
Cheng, A., Ruderman, M., & Sutherland, P. 1976, ApJ, 203, 209
Cheng, K. S., Ho, C., & Ruderman, M. 1986, ApJ, 300, 500
Chi, X., Cheng, K. S., & Young, E. C. M. 1996, ApJ, 459, L83+
Cirelli, M., Franceschini, R., & Strumia, A. 2008, Nuclear Physics B, 800, 204
Cowsik, R. & Lee, M. A. 1979, ApJ, 228, 297
Delahaye, T., Donato, F., Fornengo, N., et al. 2009, A&A, 501, 821
Delahaye, T., Lineros, R., Donato, F., Fornengo, N., & Salati, P. 2008, Phys. Rev. D, 77, 063527
Diehl, R., Halloin, H., Kretschmer, K., et al. 2006, Nature, 439, 45
Donato, F., Fornengo, N., Maurin, D., Salati, P., & Taillet, R. 2004, Phys. Rev. D, 69, 063501
Donato, F., Maurin, D., Brun, P., Delahaye, T., & Salati, P. 2009, Physical Review Letters, 102, 071301
Donato, F., Maurin, D., & Taillet, R. 2002, Astronomy and Astrophys., 381, 539
Duncan, A. R., Stewart, R. T., Haynes, R. F., & Jones, K. L. 1997, MNRAS, 287, 722
DuVernois, M. A., Barwick, S. W., Beatty, J. J., et al. 2001, ApJ, 559, 296
Ellison, D. C. & Cassam-Chenaï, G. 2005, ApJ, 632, 920
Ellison, D. C., Patnaude, D. J., Slane, P., Blasi, P., & Gabici, S. 2007, ApJ, 661, 879
Erber, T. 1966, Reviews of Modern Physics, 38, 626
Ferrière, K. M. 2001, Reviews of Modern Physics, 73, 1031
Fiasson, A., Hinton, J. A., Gallant, Y., & et al. 2008, in International Cosmic Ray Conference, Vol. 2, 719–722
Fisk, L. A. 1971, J. Geophys. Res., 76, 221
Fixsen, D. J. 2009, ArXiv e-prints
Fuerst, E., Reich, W., & Aschenbach, B. 1997, A&A, 319, 655
Furst, E., Hummel, E., Reich, W., et al. 1989, A&A, 209, 361

[5] A short summary of the workshops and the website addresses are available in Lavalle et al. (2009).

Gaensler, B. M. & Frail, D. A. 2000, Nature, 406, 158
Gaensler, B. M. & Slane, P. O. 2006, ARA&A, 44, 17
Gamezo, V. N., Khokhlov, A. M., Oran, E. S., Chtchelkanova, A. Y., & Rosenberg, R. O. 2003, Science, 299, 77
Gerardy, C. L. & Fesen, R. A. 2007, MNRAS, 376, 929
Ginzburg, V. L. & Syrovatskii, S. I. 1964, The Origin of Cosmic Rays (The Origin of Cosmic Rays, New York: Macmillan, 1964)
Ginzburg, V. L. & Syrovatskii, S. I. 1965, ARA&A, 3, 297
Gorham, P. W., Ray, P. S., Anderson, S. B., Kulkarni, S. R., & Prince, T. A. 1996, ApJ, 458, 257
Graham, D. A., Haslam, C. G. T., Salter, C. J., & Wilson, W. E. 1982, A&A, 109, 145
Green, D. A. 2005, Memorie della Societa Astronomica Italiana, 76, 534
Green, D. A. 2009, Bull. Astron. Soc. Ind., 37, 45
Harding, A. K., Stern, J. V., Dyks, J., & Frackowiak, M. 2008, ApJ, 680, 1378
Harrus, I. M., Slane, P. O., Hughes, J. P., & Plucinsky, P. P. 2004, ApJ, 603, 152
Hooper, D., Blasi, P., & Dario Serpico, P. 2009, Journal of Cosmology and Astro-Particle Physics, 1, 25
Hooper, D. & Kribs, G. D. 2004, Phys. Rev. D, 70, 115004
Humphreys, R. M. 1978, ApJS, 38, 309
Janka, H., Langanke, K., Marek, A., Martínez-Pinedo, G., & Müller, B. 2007, Phys. Rep., 442, 38
Jones, F. C. 1965, Physical Review, 137, 1306
Kamae, T., Karlsson, N., Mizuno, T., Abe, T., & Koi, T. 2006, ApJ, 647, 692
Kaplan, D. L., Chatterjee, S., Gaensler, B. M., & Anderson, J. 2008, ApJ, 677, 1201
Kaplan, D. L., Frail, D. A., Gaensler, B. M., et al. 2004, ApJS, 153, 269
Kaplan, D. L., Gaensler, B. M., Kulkarni, S. R., & Slane, P. O. 2006, ApJS, 163, 344
Katsuda, S., Petre, R., Hwang, U., et al. 2009, PASJ, 61, 155
Katsuda, S., Tsunemi, H., & Mori, K. 2008, ApJ, 678, L35
Kobayashi, T., Komori, Y., Yoshida, K., & Nishimura, J. 2004, ApJ, 601, 340
Kothes, R., Fedotov, K., Foster, T. J., & Uyanıker, B. 2006, A&A, 457, 1081
Kothes, R., Landecker, T. L., Reich, W., Safi-Harb, S., & Arzoumanian, Z. 2008, ApJ, 687, 516
Ladouceur, Y. & Pineault, S. 2008, A&A, 490, 197
Lavalle, J., Marcowith, A., & Maurin, D. 2009, in Proc. SF2A-2009, ed. M. Heydari-Malayeri, C. Reyl'E, & R. Samadi, 165–+
Lavalle, J., Nezri, E., Athanassoula, E., Ling, F.-S., & Teyssier, R. 2008a, Phys. Rev. D, 78, 103526
Lavalle, J., Pochon, J., Salati, P., & Taillet, R. 2007, A&A, 462, 827
Lavalle, J., Yuan, Q., Maurin, D., & Bi, X.-J. 2008b, A&A, 479, 427
Lazendic, J. S. & Slane, P. O. 2006, ApJ, 647, 350
Leahy, D. & Tian, W. 2006, A&A, 451, 251
Leahy, D. A., Naranan, S., & Singh, K. P. 1986, MNRAS, 220, 501
Leahy, D. A., Nousek, J., & Hamilton, A. J. S. 1991, ApJ, 374, 218
Leahy, D. A. & Tian, W. W. 2007, A&A, 461, 1013
Longair, M. S. 1994, High energy astrophysics. Vol.2: Stars, the galaxy and the interstellar medium (Cambridge: Cambridge University Press, —c1994, 2nd ed.)
Lorimer, D. R. 2004, in IAU Symposium, Vol. 218, Young Neutron Stars and Their Environments, ed. F. Camilo & B. M. Gaensler, 105–+
Lucek, S. G. & Bell, A. R. 2000, MNRAS, 314, 65
Madau, P., della Valle, M., & Panagia, N. 1998, MNRAS, 297, L17+
Malkov, M. A. & O'C Drury, L. 2001, Reports on Progress in Physics, 64, 429
Malyshev, D., Cholis, I., & Gelfand, J. 2009, Phys. Rev. D, 80, 063005
Manchester, R. N., Hobbs, G. B., Teoh, A., & Hobbs, M. 2005, AJ, 129, 1993
Mantovani, F., Nanni, M., Salter, C. J., & Tomasi, P. 1982, A&A, 105, 176
Maurin, D., Donato, F., Taillet, R., & Salati, P. 2001, ApJ, 555, 585
Mavromatakis, F. 2003, A&A, 408, 237
Mavromatakis, F., Aschenbach, B., Boumis, P., & Papamastorakis, J. 2004, A&A, 415, 1051
Mavromatakis, F., Boumis, P., Papamastorakis, J., & Ventura, J. 2002, A&A, 388, 355
Mazzali, P. A., Röpke, F. K., Benetti, S., & Hillebrandt, W. 2007, Science, 315, 825
McCullough, P. R., Fields, B. D., & Pavlidou, V. 2002, ApJ, 576, L41
Mertsch, P. & Sarkar, S. 2009, Physical Review Letters, 103, 081104
Miceli, M., Bocchino, F., & Reale, F. 2008, ApJ, 676, 1064
Morlino, G., Amato, E., & Blasi, P. 2009, MNRAS, 392, 240
Moskalenko, I. V. & Strong, A. W. 1998, ApJ, 493, 694
Mufson, S. L., McCollough, M. L., Dickel, J. R., et al. 1986, AJ, 92, 1349
Neufeld, D. A., Hollenbach, D. J., Kaufman, M. J., et al. 2007, ApJ, 664, 890
Nomoto, K., Thielemann, F., & Yokoi, K. 1984, ApJ, 286, 644
Norbury, J. W. & Townsend, L. W. 2007, Nuclear Instruments and Methods in Physics Research B, 254, 187
Odegard, N. 1986, ApJ, 301, 813
Ostriker, J. P. & Gunn, J. E. 1969, ApJ, 157, 1395
Paczynski, B. 1990, ApJ, 348, 485
Pannuti, T. G. & Allen, G. E. 2004, Advances in Space Research, 33, 434
Pesce-Rollins, M. & for the Fermi-LAT Collaboration. 2009, ArXiv e-prints
Pfeffermann, E., Aschenbach, B., & Predehl, P. 1991, A&A, 246, L28
Pieri, L., Lavalle, J., Bertone, G., & Branchini, E. 2009, ArXiv e-prints
Pineault, S., Landecker, T. L., Madore, B., & Gaumont-Guay, S. 1993, AJ, 105, 1060
Pineault, S., Landecker, T. L., Swerdlyk, C. M., & Reich, W. 1997, A&A, 324, 1152
Plucinsky, P. P., Snowden, S. L., Aschenbach, B., et al. 1996, ApJ, 463, 224
Porter, T. A., Moskalenko, I. V., Strong, A. W., Orlando, E., & Bouchet, L. 2008, ApJ, 682, 400
Profumo, S. 2008, ArXiv e-prints
Putze, A., Derome, L., & Maurin, D. 2010, ArXiv e-prints
Redman, M. P. & Meaburn, J. 2005, MNRAS, 356, 969
Reich, W., Fuerst, E., & Arnal, E. M. 1992, A&A, 256, 214
Reich, W., Zhang, X., & Fürst, E. 2003, A&A, 408, 961
Rosado, M. & Gonzalez, J. 1981, Revista Mexicana de Astronomia y Astrofisica, 5, 93
Ruderman, M. A. & Sutherland, P. G. 1975, ApJ, 196, 51
Salati, P. 2003, Physics Letters B, 571, 121
Schlickeiser, R. & Ruppel, J. 2009, ArXiv e-prints
Shaviv, N. J., Nakar, E., & Piran, T. 2009, Physical Review Letters, 103, 111302
Shen, C. S. 1970, ApJ, 162, L181+
Shikaze, Y., Haino, S., Abe, K., et al. 2007, Astroparticle Physics, 28, 154
Shinn, J., Min, K. W., Lee, C., et al. 2006, ApJ, 644, L189
Shinn, J.-H., Min, K. W., Sankrit, R., et al. 2007, ApJ, 670, 1132
Silk, J. & Srednicki, M. 1984, Physical Review Letters, 53, 624
Sofue, Y., Furst, E., & Hirth, W. 1980, PASJ, 32, 1
Strom, R. G. & Stappers, B. W. 2000, in Astronomical Society of the Pacific Conference Series, Vol. 202, IAU Colloq. 177: Pulsar Astronomy - 2000 and Beyond, ed. M. Kramer, N. Wex, & R. Wielebinski, 509–+
Strong, A. W. & Moskalenko, I. V. 1998, ApJ, 509, 212
Strong, A. W., Moskalenko, I. V., & Ptuskin, V. S. 2007, Annual Review of Nuclear and Particle Science, 57, 285
Strong, A. W., Moskalenko, I. V., & Reimer, O. 2000, ApJ, 537, 763
Stupar, M., Parker, Q. A., & Filipović, M. D. 2007, MNRAS, 374, 1441
Sturrock, P. A. 1970, Nature, 227, 465
Sturrock, P. A. 1971, ApJ, 164, 529
Sun, X. H., Reich, W., Han, J. L., Reich, P., & Wielebinski, R. 2006, A&A, 447, 937
Tan, L. C. & Ng, L. K. 1983, Journal of Physics G Nuclear Physics, 9, 1289
Tatischeff, V. 2009, A&A, 499, 191
Taylor, A. R., Gibson, S. J., Peracaula, M., et al. 2003, AJ, 125, 3145
Taylor, J. H., Manchester, R. N., & Lyne, A. G. 1993, ApJS, 88, 529
Troja, E., Bocchino, F., Miceli, M., & Reale, F. 2008, A&A, 485, 777
Uyaniker, B., Kothes, R., & Brunt, C. M. 2002, ApJ, 565, 1022
Valinia, A. & Marshall, F. E. 1998, ApJ, 505, 134
van den Bergh, S. & Tammann, G. A. 1991, ARA&A, 29, 363
Vinyaikin, E. N. 2007, Astronomy Reports, 51, 570
Welsh, B. Y. & Sallmen, S. 2003, A&A, 408, 545
Welsh, B. Y., Sfeir, D. M., Sallmen, S., & Lallement, R. 2001, A&A, 372, 516
Woosley, S. & Janka, T. 2005, Nature Physics, 1, 147
Xiao, L., Fürst, E., Reich, W., & Han, J. L. 2008, A&A, 482, 783
Xiao, L., Reich, W., Fürst, E., & Han, J. L. 2009, ArXiv e-prints
Yar-Uyaniker, A., Uyaniker, B., & Kothes, R. 2004, ApJ, 616, 247

Yüksel, H., Kistler, M. D., & Stanev, T. 2009, Physical Review Letters, 103, 051101
Yusifov, I. & Küçük, I. 2004, A&A, 422, 545
Zeiger, B. R., Brisken, W. F., Chatterjee, S., & Goss, W. M. 2008, ApJ, 674, 271
Zhang, L. & Cheng, K. S. 2001, A&A, 368, 1063

Appendix A: Analytical solutions for the spatial integral

Here, we briefly give the solutions for the spatial integral of the Green function convoluted with a disk-like spatial distribution for sources. We will distinguish two cases: (i) a homogeneous flat disk, which is relevant for secondary CR electrons and positrons (see Eq. 37), and (ii) a z-exponential disk (see Eq. 47), relevant for primaries as long as the actual distribution of sources does not exhibits too strong gradients over a distance fixed by the half-thickness of the diffusion zone $\sim L$.

In both cases, disregarding the radial boundary conditions, the radial solution is quite simple:

$$\begin{aligned}\mathcal{I}_r &\equiv \int_{r_{\rm min}}^{r_{\rm max}} dr_s\, r_s\, \frac{\exp\left\{-\frac{r_s^2}{\lambda^2}\right\}}{\pi\,\lambda^2} \qquad (A.1)\\ &= \frac{\exp\left\{-\frac{r_{\rm min}^2}{\lambda^2}\right\}}{2\,\pi}\left[1-\exp\left\{-\frac{r_{\rm max}^2-r_{\rm min}^2}{\lambda^2}\right\}\right]\\ &\stackrel{\substack{r_{\rm max}\to\infty\\ r_{\rm min}\to 0}}{\longrightarrow} \frac{1}{2\,\pi}\,.\end{aligned}$$

If one wants to take into account the radial boundary, it is enough to add a second propagator that will cancel out the first one at $r = R$. The 2D-propagator becomes:

$$\mathcal{G}_r(\boldsymbol{r}_\odot, E \leftarrow \boldsymbol{r}_s, E_s) = \frac{1}{\pi\,\lambda^2}\left(\exp\left\{-\frac{(\boldsymbol{r}_\odot-\boldsymbol{r}_s)^2}{\lambda^2}\right\} - \exp\left\{-a(r_s)\frac{(\boldsymbol{r}_\odot-\boldsymbol{r}_{im})^2}{\lambda^2}\right\}\right) \qquad (A.2)$$

where the image satisfies $\boldsymbol{r}_{im} = \boldsymbol{r}_s/a(r_s)$ with the scale parameter $a(r) = \frac{r^2}{R^2}$. This is actually equivalent with replacing $R_\odot$ by $\frac{R^2}{R_\odot}$ and λ by $\lambda\frac{R}{R_\odot}$ (except for the first λ^2 that is in factor). In the case of secondary production, when the source term is homogeneous in the disk, the integration over the total disk is analytical and gives:

$$\begin{aligned}\mathcal{I}^{\rm hom}_{r,\theta} &= \int_0^{2\pi}\int_0^R r\mathcal{G}_r(\boldsymbol{r}, E\leftarrow\boldsymbol{r}_s, E_s)\,dr d\theta =\\ &e^{-\frac{R_\odot^2}{\lambda^2}}\sum_{m=0}^{\infty}\left\{\left(\frac{R_\odot^2}{\lambda^2}\right)^m\frac{1}{m!}\left(1-e^{-\frac{R^2}{\lambda^2}}\sum_{j=0}^{m}\left(\frac{R^2}{\lambda^2}\right)^j\frac{1}{j!}\right)\right\}\\ &-\frac{e^{-\frac{R^2}{\lambda^2}}}{a(R_\odot)}\sum_{m=0}^{\infty}\left\{\left(\frac{R^2}{\lambda^2}\right)^m\frac{1}{m!}\left(1-e^{-\frac{R_\odot^2}{\lambda^2}}\sum_{j=0}^{m}\left(\frac{R_\odot^2}{\lambda^2}\right)^j\frac{1}{j!}\right)\right\}.\end{aligned}$$

A.1. Vertical solution for the homogeneous disk approximation

Here, we just quote the result already obtained in Delahaye et al. (2009) for secondary positrons. We have:

$$\begin{aligned}\mathcal{I}_z^{\rm hom} &= \int_{-z_{\rm max}}^{z_{\rm max}} dz_s\,\mathcal{G}_z(\lambda, z=0\leftarrow z_s) \qquad (A.3)\\ &= \begin{cases}\dfrac{1}{2}\displaystyle\sum_{n=-\infty}^{\infty}\left\{\mathrm{erf}\left(\frac{z_n^{\rm max}}{\lambda}\right)-\mathrm{erf}\left(\frac{z_n^{\rm min}}{\lambda}\right)\right\}\,,\\ \dfrac{2}{L}\displaystyle\sum_{n=1}^{\infty}(-1)^{n+1}\frac{\cos\left(k_n(L-z_{\rm max})\right)}{k_n}\times e^{-k_n^2\lambda^2/4}\,.\end{cases}\end{aligned}$$

The latter case corresponds to the Helmholtz solution, while the former one is the image solution, for which we have $z_n^{\rm max}\equiv 2nL+(-1)^n z_{\rm max}$ and $z_n^{\rm min}\equiv 2nL-(-1)^n z_{\rm max}$. Throughout the paper, we have used a disk of half-thickness $z_{\rm max} = h = 0.1$ kpc.

A.2. Vertical solution for the z-exponential disk approximation

If we consider sources which exhibit an exponential vertical profile, the integral has to be performed over the complete diffusion zone:

$$\mathcal{I}_z^{\rm exp} = \int_{-L}^{L} dz_s\,\mathcal{G}_z(\lambda, z=0\leftarrow z_s)e^{(-|z|/z_0)} = \qquad (A.4)$$
$$\begin{cases}\displaystyle\sum_{n=-\infty}^{\infty}(-1)^n e^{b_n^2-\left(\frac{2nL}{\lambda}\right)^2}\left\{\mathrm{erf}\left(\frac{L}{\lambda}+b_n\right)-\mathrm{erf}\left(b_n\right)\right\}\,,\\ \dfrac{2}{L}\displaystyle\sum_{n=1}^{\infty}\left((-1)^{n+1}z_0k_n e^{-L/z_0}+1\right)\times\frac{z_0 e^{-k_n^2\lambda^2/4}}{1+z_0^2k_n^2}\,.\end{cases}$$

The first case corresponds to the image solution and b_n stands for $\frac{\lambda}{2z_0}+(-1)^n\frac{2nL}{\lambda}$. The second case corresponds to the Helmholtz solution.

Appendix B: Fitting formulae for secondary electrons and positrons

Here, we provide useful fitting formulae for our template computations of the interstellar secondary flux, for both CR electrons and positrons, in the *med* propagation setup and with the M1 ISRF model for the full relativistic energy losses (see Sect. 2.5 and Sect. 3 for more details). These formulae do not account for the solar modulation that the user will have to implement by oneself, and are relevant from $\sim$ 1 GeV up to a few TeV. We will use the following parameterization for the flux, as expressed in units of $(\mathrm{GeV\,cm^2\,s\,sr})^{-1}$:

$$\phi_{\rm sec}(E) = \exp\left\{\sum_{i=0}^{N}\alpha_i\left[\ln\left(\frac{E}{1\,\mathrm{GeV}}\right)\right]^i\right\}\,. \qquad (B.1)$$

For secondary positrons, we find:

$$\begin{aligned}\alpha_i^{e^+} &= \Big\{-5.46298, -3.52896, -0.0887432, 0.0319396,\\ &\quad -0.00339393, 0.000107393\Big\}\,, \qquad (B.2)\end{aligned}$$

while for electrons, we have:

$$\alpha_i^{e^-} = \Big\{ -6.00407, -3.40715, -0.0977409, 0.0346854, -0.00441225, 0.00019 \Big\}. \quad \text{(B.3)}$$

Note that rescaling these formulae by a global factor mostly means rescaling the averaged local value of the gas density in the disk.

Appendix C: Local Supernova Remnants

SNRs are very numerous but not always easy objects to detect. The most complete available catalog is the one from Green (2005). It has been recently updated (Green 2009). Moreover the recent Canadian Galactic Plane Survey (Taylor et al. 2003, CGPS hereafter) has focused on many of these objects. In the following we discuss the SNRs that lie less than ~ 2 kpc away from the Earth. We have classified them by distance to the Earth. All the important data we have used are summed up in Tab. C.1. Considering the number of recent discoveries in this region, it is more than probable that others remnants will be discovered in the future.

It clearly appears from Fig. 9 that all sources do not contribute the same way. We first list here only the most important ones.

G203.0+12.0-3.3 Also called Monogem ring, this object is considered as a "probable remnant" by the Green catalog. Results based on observations from Plucinsky et al. (1996) derived a distance of ~ 300 pc and an age of 86 kyr. Parallax measurements by Brisken et al. (2003) for the associated pulsar gave a more precise distance of 288^{+33}_{-27} pc. Being 25° in diameter in the sky, it is impossible to infer neither a correct power spectrum nor a brightness.

G263.9-3.3 This SNR is one of the brightest radio object in the sky. Its apparent big size was the reason it was long thought three different objects of the Vela constellation, and this is why it is often called Vela (XYZ). Cha et al. (1999) have estimated its distance to be 250 ± 30 pc by absorption measurements. This is consistent with the parallax measurement of the associated pulsar (PSR) B0833–45 from Caraveo et al. (2001) which gave 294^{+76}_{-50} pc. Pulsar period derivative and nebula evolution lead to the same age of $\sim 11{,}200$ yr (Taylor et al. 1993; Miceli et al. 2008). Radio observations review from Alvarez et al. (2001) gave the three spectral indices of the structure: $\alpha_X = 0.39 \pm 0.03$, $\alpha_Y = 0.70 \pm 0.10$, and $\alpha_Z = 0.81 \pm 0.16$. They also gave brightnesses at 1 GHz of each parts: $S_X = 1,160 \pm 200$ Jy, $S_Y = 440 \pm 240$ Jy, and $S_Z = 400 \pm 260$ Jy, which in total gives $S_{XYZ} = 2,000 \pm 700$ Jy which is consistent with the value of 1,750 Jy given by Green (2009).

Antlia Although not yet in Green catalog, this remnant has recently been discovered by McCullough et al. (2002) and confirmed by Shinn et al. (2007). It lies at coordinates 276.5+19.0 and at a distance of only 60-340 pc from the Sun (Sedov estimation). Other considerations (maximal size, column density and ^{26}Ti abundance) favors the lower bound of the distance. Its age is probably more than 1 Myr. However its angular diameter is so large (24°) that a correct spectral index cannot be inferred.

Hereafter are listed other nearby SNRs ($\leq$2. kpc). Some authors did not correct their age estimations by the light travel length, sometimes leading to results outside our light-cone. Therefore, a supplemental uncertainty of $\Delta d/c$ on the age should be added in some cases.

G18.95-1.1 Using HI absorption observations, Furst et al. (1989) estimated its distance to the Earth to ~ 2 kpc, but they could not exclude the possibility that it could be an extremely and unusually bright object located 15 kpc away. The most recent study from Harrus et al. (2004) estimated the age of the object at 4,400 to 6,100 yr (without taking into account the distance uncertainty). However this value is inconsistent with causality constraints, so we have added the value corresponding to the distance: 6.5 kyr. Using ROSAT observation, Fuerst et al. (1997) found a spectral index of 0.28 but the remnant is hosting many substructure that makes this value difficult to appreciate. They also give a luminosity of order 40 Jy at 1 GHz.

G65.3+5.7 Sometimes this remnant is also called G65.2+5.7. The radio power spectrum is 0.58 ± 0.07 from 83 MHz up to 4.8 GHz (Xiao et al. 2009), and the estimated distance varies from 800 pc to 1 kpc. In earlier studies, in the context of a pulsar survey in several SNRs (Gorham et al. 1996), among which G65.2+5.7, the flux is estimated to 52 Jy at 1 GHz, but this last quantity is rough estimated. Optical observation from Mavromatakis et al. (2002) leads to an age of ~ 26 kyr.

G67.5+1.2 Also called DA 495, this object is highly polarized. Kothes et al. (2006) suggest that point-like sources may alter the measurement of the power spectrum, leading in that case to a lower limit of 0.38 ± 0.08. The brightness at 1 GHz they have obtained is 4.6 ± 0.2 Jy which should be considered as an upper limit since the remnant seems to sit on a diffuse emission plateau. However, a more recent work from Kothes et al. (2008) seems to indicate that it is not a shell-type SNR but a PWN. Indeed the spectrum has a power break at ~ 1.3 GHz and no shell. The power spectrum is 0.45 ± 0.1 and the spectral break is of 0.42 ± 0.22. The corresponding brightness is of order ~ 5 Jy at 1 GHz. They also give a distance of 1.0 ± 0.4 kpc and an age of 20,000 yr. However, if there is a pulsar in this remnant, it has not been detected yet.

G69.0+2.7 More often called CTB 80, this remnant is estimated by Castelletti et al. (2003) to be $\sim 20{,}000$ yr old. Multi-frequency review from Castelletti & Dubner (2005) gives a spectral index of 0.36 ± 0.02 and a brightness of ~ 65 Jy at 1 GHz. However, the more recent Canadian Galactic plane survey (Kothes et al. 2006) gives a spectrum of 0.2 ± 0.1 and a brightness of 60 ± 10 Jy. Many authors cite Strom & Stappers (2000) as a reference for a distance of ~ 2 kpc based on HI absorption observations. The study by Zeiger et al. (2008) seems to reveal an associ-

#	SNR G+long+lat	other name	distance [kpc]	radio index	Brightness [Jy]	age [kyr]	Pulsar
1	18.95-1.1		2. ± **0.1**	0.28	40	11.75 ± 0.85	?
2	65.3+5.7		0.9 ± 0.1	0.58 ± 0.07	52	26 ± **1**	∅
3	65.7+1.2	DA 495	1.0 ± 0.4	0.45 ± 0.1	5	16.75 ± 3.25	unknown
4	69.0+2.7	CTB 80	2.0 ± **0.1**	0.20 ± 0.10	60 ± 10	20 ± **1**	J1952+3252
5	74.0-8.5	Cygnus Loop	$0.54^{+0.10}_{-0.08}$	0.4 ± 0.06	175 ± 30	10 ± **1**	∅
6	78.2+2.1	γ Cygni	1.5 ± **0.1**	0.75 ± 0.03	275 ± 25	7 ± **1**	∅
7	82.2+5.3	W63	2.3 ± 1.0	0.36 ± 0.08	105 ± 10	20.1 ± 6.6	∅
8	89.0+4.7	HB 21	1.7 ± 0.5	0.27 ± 0.07	200 ± 15	5.60 ± 0.28	∅
9	93.7-0.2	CTB 104A or DA 551	1.5 ± 0.2	0.52 ± 0.12	42 ± 7	50 ± 20	∅
10	114.3+0.3		0.7	0.49 ± 0.25	6.4 ± 1.4	7.7 ± **0.1**	∅
11	116.5+1.1		1.6	0.16 ± 0.11	10.9 ± 1.2	20 ± 5	B2334+61 ?
12	116.9+0.2	CTB 1	1.6	0.33 ± 0.13	6.4 ± 1.4	20 ± 5	B2334+61 ?
13	119.5+10.2	CTA 1	1.4 ± 0.3	0.57 ± 0.06	42.5 ± 2.5	10 ± 5	J0010+7309
14	127.1+0.5	R5	1.±0.1	0.43 ± 0.1	12 ± 1	25 ± 5	∅
15	156.2+5.7		0.8 ± 0.5	$2.0^{+1.1}_{-0.7}$	4.2 ± 0.1	10 ± **1**	B0450+55 ?
16	160.9+2.6	HB 9	0.8 ± 0.4	0.48 ± 0.03	∼ 75	5.5 ± 1.5	B0458+46
17	180.0-1.7	S147	1.2 ± 0.4	0.75	74 ± 12	600 ± **10**	J0538+2817
18	184.6-5.8	Crab nebula or 3C144 or SN1054	2.0 ± 0.5	0.3	1,040	7.5 ⋆	B0521+31
19	189.1+3.0	IC 443	1.5 ± **0.1**	0.36 ± 0.04	160 ± 5	30 or 4	∅
20	203.0+12.0	Monogem ring	$0.288^{+0.033}_{-0.027}$			86 ± **1**	B0656+14
21	205.5+0.5	Monoceros Nebula	1.63 ± 0.25	0.66 ± 0.2	156.1 ± 19.9	29 ± **1**	∅
22	263.9-3.3	Vela(XYZ)	0.295 ± 0.075	variable	2,000 ± 700	11.2 ± **0.1**	B0833-45
23	266.2-1.2	RX J0852.0-4622 or Vela Jr or SN1300	0.75 ± **0.01**			3.5 ± 0.8 ⋆?	J0855-4644 ?
24	276.5+19.0	Antlia	0.2 ± 0.14			≥ 1,000	B0950+08
25	315.1+2.7		1.7 ± 0.8	0.7		**50** ± **10**	J1423-56
26	330.0+15.0	Lupus Loop	1.2 ± 0.3			50 ± **10**	B1507-44 ?
27	347.3-0.5	SN393	1.± 0.3			4.9 ⋆	∅

Table C.1. Characteristics of nearby SNRs. Spectral index and Brightness are inferred from measurements made at 1 GHz. Uncertainties in bold are not taken from bibliographic references, but just correspond to a rough uncertainty on the last relevant digit; hence they can be underestimated. An age is flagged with a ⋆ for an historical remnant; in this case, the age uncertainty is set from the distance uncertainty. Note that these ages are the *observed* ages, which differ from the *actual* ages by d/c.

ation with the pulsar B1951+32. However it might be much older (51 kyr) than the remnant.

G74.0-8.5 Also known as Cygnus Loop this ∼ 10,000 yr old remnant has been shown by Blair et al. (2009) to be farther than 576 ± 61 pc away. This is consistent with Hubble Space Telescope observations from Blair et al. (2005) which found 540^{+100}_{-80} pc. Sun et al. (2006) found a spectral index of 0.40 ± 0.06 and an integrated flux of 175 ± 30 Jy at 1 GHz.

G78.2+2.1 This remnant is also called γ Cygni. The catalog based on the CGPS gives a brightness of 275 ± 25 Jy at 1 GHz taking into account more recent work of Ladouceur & Pineault (2008), which yields a very precise spectral index of 0.75 ± 0.03 that correctly takes into account the thermal subtraction. Deep optical survey from Mavromatakis (2003) revealed an age of ∼ 7,000 yr. However it is not possible from HI observation to infer a distance, depending on the method they find either 1 or 4 kpc with big error bars. The value of 1.5 kpc seems to preferred by most recent authors (see Bykov et al. 2004, and references therein).

G82.2+5.3 Also called W63, this remnant is estimated by Mavromatakis et al. (2004) at a distance between 1.6 and 3.3 kpc and an age between 13.5 and 26.7 kyr. However it is not clear whether the Sedov analysis they have performed is licit in this case. Previous review from Rosado & Gonzalez (1981) suggests a distance of 1.6 ± 0.3 kpc. The catalog based on the CGPS gives a brightness of 105 ± 10 Jy at 1 GHz and a spectral index of 0.36 ± 0.08.

G89.0+4.7 According to Byun et al. (2006), this remnant, also known as HB 21, is at a distance of 1.7 ± 0.5 kpc from the Sun. The review from Reich et al. (2003) suggests a spectral index of 0.41 ± 0.02 and a flux density of 228 ± 5 Jy at 1 GHz. However, the more recent CGPS gives an index of 0.27 ± 0.07 and a brightness of 200 ± 15 Jy. A study from Lazendic & Slane (2006) estimates the age to 5,600 ± 280 yr but they used the former distance estimation of 0.8 kpc by Humphreys (1978) ; it is not clear how this age would change for a larger distance of 1.7 kpc.

G93.7-0.2 Also referred to as CTB 104A or DA 551, this highly polarized and large object has been studied by Kothes et al. (2006). They measured a spectral index of 0.52 ± 0.12 and a brightness at 1 GHz of 42 ± 7 Jy. Uyaniker et al. (2002) estimated its distance at 1.5 ± 0.2 kpc but in Kothes et al. (2006), citing the same reference, the authors give 1.4 kpc. The only age estimation we could find is the one from Mantovani et al. (1982),

which suggests 29,000 to 74,000 yr. However most of the other results of these observations have been corrected by later works and therefore it is not clear to us how trustworthy this age estimation is.

G114.3+0.3 Although some authors (see *e.g.* Kaplan et al. 2006) still use the large value of 3.5 kpc, recent HI association from Yar-Uyaniker et al. (2004) gives 0.7 kpc. Same authors also estimated an age of 7,700 yr. Because of its proximity to Cas A, Kothes et al. (2006) were not able to measure the flux and the spectral index. However, they give, as an average of previous works, a spectral index of 0.49 ± 0.25 and a flux of 6.4 ± 1.4 Jy at 1 GHz.

G116.5+1.1 While some authors (see *e.g.* Kaplan et al. 2006) still use the large value of 4 kpc, recent HI association from Yar-Uyaniker et al. (2004) gives 1.6 kpc. Same authors also estimated its age to be between 15,000 and 50,000 yr preferring a younger age. We decided to take 20 ± 5 kyr. Kothes et al. (2006) measured a spectral index of 0.16 ± 0.11 and a flux of 10.9 ± 1.2 Jy at 1 GHz. It is possible that the pulsar B2334+61 is associated to this remnant (or to the next one) however the age and distance estimations given by the ATNF catalog (Manchester et al. 2005) do not match very well.

G116.9+0.2 Also called CTB 1, this remnant is considered by some authors (see *e.g.* Kaplan et al. 2006) to lie 3.1 kpc away. However recent HI association from Yar-Uyaniker et al. (2004) gives 1.6 kpc. It seems that it is very close to G116.5+1.1. Same authors also estimated its age to be between 15,000 and 50,000 yr preferring a younger age. Kothes et al. (2006) measured a spectral index of 0.33 ± 0.13 and a flux of 7.9 ± 1.3 Jy at 1 GHz.

G119.5+10.2 Also known as CTA1, this remnant is the first object seen by Fermi (Abdo et al. 2008). The most recent estimation of it age and distance are from Pineault et al. (1993) who estimated the distance to be 1.4 ± 0.3 kpc and the age to be between 5,000 and 15,000 yr. The later study of Pineault et al. (1997) revealed a spectral index of 0.57 ± 0.06 and a brightness of $40 \sim 45$ Jy at 1 GHz.

G127.1+0.5 Also known as R 5, this remnant has recently been studied by Leahy & Tian (2006) who used radio observation from the CGPS. They determined an age of 2–3 10^4 yr, a spectral of 0.43 ± 0.10 and a brightness of 12 ± 1 Jy at 1 GHz. For the distance, thanks to HI line survey, they found 1.15 kpc which is consistent with an association with NGC 559, located 0.9–1.13 kpc away from the Sun.

G156.2+5.7 Discovered during ROSAT survey by Pfeffermann et al. (1991), this remnant is one of the faintest in the Galaxy with a brightness of 4.2 ± 0.1 Jy at 1 GHz (see *e.g.* Reich et al. 1992). In their study of the X-ray emission, Pannuti & Allen (2004) have found that the photon emission is in agreement with an electron density with a power law of $2.0\ ^{+1.1}_{-0.7}$ and a cut-off at about 10 TeV. Its distance from the Sun was first estimated to a few pc, however, it seems from optical study by Gerardy & Fesen (2007) that the remnant may be as close as 300 pc and younger than 10,000 yr. In their latest paper, Katsuda et al. (2009) use 1 kpc.

G160.9+2.6 Also called HB9, the recent study of Leahy & Tian (2007) based on the CGPS and HI observations gives a spectral index of 0.48 ± 0.03, and a distance of 0.8 ± 0.4 kpc. Concerning the age, they conclude that the Sedov age for HB9 is 6,600 yr and the evaporative cloud model yields ages of 4,000 – 7,000 yr. However, the age of the corresponding pulsar B0458+46 seems to be 7 kyr. The brightness is of order 75 Jy at 1 GHz.

G180.0-1.7 This bright radio remnant is also called S147. The 143 ms pulsar PSRJ0538+2817 (Anderson et al. 1996) is located within S147 and believed to be associated as the distance estimates for both the remnant (0.8–1.6 kpc) and the pulsar (1.2 kpc) agree. The characteristic age of the pulsar of 600 kyr is much larger than the estimated 100 kyr based on radio data from Sofue et al. (1980). However the complexity of the environment of this remnant make any age analysis extremely difficult. Therefore we will adopt the age of the pulsar. Reich et al. (2003) measured the brightness of the source at 863 MHz. Using the spectral index of 0.30 ± 0.15 from Xiao et al. (2008), one finds a brightness of 74 ± 12 Jy at 1 GHz. Xiao et al. (2008) also showed that the spectrum is broken at ~ 1.5 GHz above which the index increases to 1.35 ± 0.20; this is probably due to the diffuse component.

G184.6-5.8 One of the most famous, more known as Crab nebula or 3C144, this is the remnant of the historical Supernova SN1054. As very well explained in Kaplan et al. (2008), even though this object is used to calibrate many instruments and hence very well studied, its exact distance cannot be measured precisely because its impressive brightness prevents from a parallax study. The nominal distance in the literature is 2.0 ± 0.5 kpc. The corresponding age is therefore 6,000 to 9,000 yr. According to the Green catalog its spectral index is ~ 0.3 and it brightness is 1,040 Jy at 1 GHz. However, Vinyaikin (2007) have shown that this value is decreasing with time.

G189.1+3.0 Also named IC 443, this 30,000 yr old remnant is well-known for its rich chemical composition (see Neufeld et al. 2007, and references therein). Welsh & Sallmen (2003) have calculated a distance of $\sim$ 1.5 kpc. The review by Mufson et al. (1986) gives a power spectrum of 0.36 ± 0.04 and Reich et al. (2003) provide an intensity of 160 ± 5 Jy. A recent observation from XMM-Newton (Troja et al. 2008) gives a much younger age of 4,000 yr.

G205.5+0.5 Also known as Monoceros Nebula or the Monoceros Loop, this SNR is believed to be associated to the Rosette Nebula (see Odegard 1986) which lies at a distance of 1.6 ± 0.2 kpc from the Sun (Bonatto & Bica 2009). This special position makes it a very interesting probe for cosmic ray acceleration study (see Fiasson et al. 2008). Leahy et al. (1986) have estimated the age of the object to

$\sim$ 29,000 yr. However, this value is very model-dependent, and ultraviolet spectroscopy analysis by Welsh et al. (2001) suggests that it is even older (up to 150,000 yr). The review from Graham et al. (1982) suggests a spectral index of 0.47 $\pm$ 0.06 for the radio emission and a flux density of 156.1 $\pm$ 19.9 Jy at 1 GHz. More recent results from Borka Jovanović & Urošević (2009) with higher statistics prefer an index of 0.66 $\pm$ 0.20 with a brightness at 1 GHz in agreement with previous ones and a distance of 1,630 $\pm$ 250 pc.

G266.2-1.2 Often referred to as RX J0852.0-4622 or Vela Junior, the detection of the radioactive decay line of ^{44}Ti seems to prove that it is a very young object. However its proximity with Vela makes any estimation of it brightness and spectral index quite difficult. The most recent study from Katsuda et al. (2008), based on evolution study, estimated its age between 2,700 and 4,300 yr and its distance to $\sim$ 750 pc. It is a little puzzling that no historical record of this supernova explosion, that happened around year 1,300, has been found. It was proposed in Redman & Meaburn (2005) an association with pulsar PSR J0855-4644, based on a reestimate of the pulsar distance.

G315.1+2.7 Recent discovery by Stupar et al. (2007) of this extremely large remnant revealed a distance of $\sim$1.7 kpc. Reanalyzing the former radio observation by Duncan et al. (1997) they found a spectral index of 0.7. However it seems that some ambiguity remains concerning the brightness. The age is not given precisely but it is considered as old. Without anymore precision we have taken 50 $\pm$ 10 kyr.

G330.0+15.0 Also called Lupus Loop, this remnant is 800 pc away from the Sun (Kaplan et al. 2004). However, a recent review by Shinn et al. (2006) gives 1.2 $\pm$ 0.4 kpc. According to Kaplan et al. (2006) (and references therein) it is 50 kyr old. Very few data are available for Lupus Loop in radio wavelength. To our knowledge, the latest are from Leahy et al. (1991), who concluded that its spectrum could not be featured by a single power law.

G347.3-0.5 Associated with the gamma source RX J1713.7-3946, this SNR lies about 1 kpc away. The age of the first light on Earth is estimated to be $\sim$ 1,600 yr, consistent with the historical Chinese record of an SN exploded in AD 393 (see *e.g.* Morlino et al. 2009). For a distance of $\sim$ 1kpc away, this means an age of $\sim$ 4.9 kyr. Ellison & Cassam-Chenaï (2005) explained that because its environment is extremely complex, it is very difficult to subtract background and to deduce neither power spectrum nor brightness.